



City Research Online

City St George's, University of London

Citation: Qian, K., Lan, X., Li, Z., Li, Y. & Fu, F. (2020). Progressive Collapse Resistance of Two-Storey Seismic Configured Steel Sub-Frames Using Welded Connections. *Journal of Constructional Steel Research*, 170, 106117. doi: 10.1016/j.jcsr.2020.106117

This is the accepted version of the paper.

This version of the publication may differ from the final published version. To cite this item please consult the publisher's version.

Permanent repository link: <https://openaccess.city.ac.uk/id/eprint/24060/>

Link to published version: <https://doi.org/10.1016/j.jcsr.2020.106117>

Copyright and Reuse: Copyright and Moral Rights remain with the author(s) and/or copyright holders. Copies of full items can be used for personal research or study, educational, or not-for-profit purposes without prior permission or charge, unless otherwise indicated, provided that the authors, title and full bibliographic details are credited, a hyperlink and/or URL is given for the original metadata page and the content is not changed in any way. For full details of reuse please refer to [City Research Online policy](#).

1

2 **Progressive Collapse Resistance of Two-Storey Seismic Configured Steel Sub-**

3 **Frames Using Welded Connections**

4 Kai Qian^{1*}, Xi Lan¹, Zhi Li¹, Yi Li², Feng Fu³

5 ¹College of Civil Engineering and Architecture, Guangxi University, Nanning, China, 530004.

6 ² Key Lab. of Urban Security and Disaster Engineering of Ministry of Education, Beijing University of Technology,
7 Beijing 1000124, China

8 ³ School of Mathematics, Computer Science and Engineering, City, University of London, London, EC1V 0HB UK.

9 **Abstract:**

10 This paper presents the experimental and numerical investigation on resistance of two-storey steel
11 sub-frames subjected to a middle column removal scenario. Two different types of 1/2 scaled steel
12 sub-frames with seismic configuration were fabricated and tested, they are: (1) welded connections
13 with gross beam section (GBS) and (2) welded connections with reduced beam section (RBS,
14 typically used for energy dissipation in earthquake design). Based on the test results, finite element
15 models using explicit software LS-DYNA which can accurately replicate the response of the frames
16 were created and validated. Using the validated model, the parametric studies were also performed to
17 investigate the effect of different parameters on the progressive collapse resistance of the frame. Base
18 on the experimental and numerical studies, the failure mechanism and collapse resistance capacities
19 of these two types of frame systems are first time investigated. The test results indicated that the
20 welded connections with RBS exhibits better performance due to the guaranteed formation of plastic
21 hinges at the location of reduced section, as well as the avoidance of welding heat effect and brittle
22 weld fracture at beam to column connections. Thus, RBS exhibits larger deformation capacity which
23 is favorable in mitigating the possible progressive collapse.

24 **Keywords:** Experimental; Numerical; Multi-Storey; Progressive Collapse; Steel; Weld Connection

25 * Corresponding author. Tel.: 86+771-3232894, E-mail address: qiankai@gxu.edu.cn

26 **1. Introduction**

27 Progressive collapse refers to a situation in which the failure of a local failure causes a major
28 collapse, with the magnitude being disproportionate to the initial event. In recent years, the increasing
29 terrorist attacks have increased the likelihood of progressive collapse. Due to its catastrophic
30 consequences, progressive collapse has been the focus of engineers and researchers in the civil
31 engineering research community.

32 Progressive collapse is a dynamic event, and many studies have examined the dynamic collapse
33 performance. Previous studies have introduced the strain rate effects in dynamic progressive collapse
34 analysis [1-2]. It has been reported that the strain rate effects could change the failure mechanism of
35 the connections and influence the capacity of progressive collapse. To approximately compensate for
36 dynamic effects when a static procedure is used, many procedures and explicit expressions have been
37 proposed [3-5] and dynamic increase factor was investigated [6-8]. Ferraioli [9] developed a modal
38 pushdown analysis procedure for progressive collapse assessment of multi-storey steel frame
39 buildings under sudden removal scenario of a column due to catastrophic events. For steel frames,
40 catenary action (CA) is an essential load resisting mechanism to redistribute the loads after column
41 removal [10-11].

42 However, more researchers use static procedure during the test due to the difficulty in performing
43 the dynamic tests. Some of existing tests are relied on two-dimensional tests replicate whole beam
44 span and portions of structural frame were designed as boundary conditions [12-15]. Lew et al. [12]
45 conducted an experimental study of two steel moment frame under a column-removal scenario, to
46 investigate the behavior and failure modes of steel joints including the development of catenary
47 action. Majority of these test specimens were only half beam span and the extremity of connections
48 was pinned which was a simplified boundary condition [16-20]. Yang and Tan [16] presented seven
49 experimental tests on the performance of common types of bolted steel beam-column joints under a
50 central-column-removal scenario subjected to catenary action, and it indicated that tensile capacities
51 of beam-column joints after undergoing large rotations usually control the failure mode and the
52 formation of catenary action. Li et al. [17] investigated behavior of two steel joints subjected to

53 column loss and effective catenary action was developed in both specimens. The effects of slab
54 flange were also considered [21-28].

55 Although several studies had been carried out on progressive collapse resistance of steel sub-
56 assemblages with different types of connections, studies especially tests on multi-story beam-column
57 sub-frames were still scarce. Li et al. [29-30] carried out a series test of two-bay by two-story steel
58 frame with welded connections subjected to sudden column removal scenario. It was found that the
59 mobilization of catenary action in the first story was more significant than that of second story. Thus,
60 assuming all upper stories above the lost column performed similarly and developing equally load
61 resistance may be not accurate. It was necessary to carry out multi-story frame tests for deep
62 understanding the behavior of steel frames subjected to the loss of column scenarios. To tackle this
63 problem, in this paper, a series of two two-story by two-bay half-scale steel sub-frames using welded
64 connections with seismic configuration were fabricated and tested. In this study, a quasi-static
65 loading scheme is adopted and strain rate effects are not considered. Based on the test results, finite
66 element models using explicit software LS-DYNA which can accurately replicate the response of the
67 frames are created and validated. Using the validated model, the parametric studies are also
68 performed to investigate the effect of different parameters on the progressive collapse resistance of
69 the frame.

70 2. Experimental program

71 2.1. Test specimens

72 As shown in Fig. 1, the prototype frame was a six-story steel frame with six bays in both
73 longitudinal and transverse directions. The span in longitudinal and transverse directions was 8.4 m
74 and 6.0 m, respectively. The specimen was designed in accordance with seismic design requirements
75 of AISC-341 [31]. The design dead and live loads were 5.1 kN/m² and 3.0 kN/m², respectively. The
76 connections were designed in accordance to FEMA 350 [32]. Only two-bay by two-story sub-frame
77 was extracted from the prototype frame for experimental tests for a middle column lost. Owing to
78 space, facility and cost limitation, only half-scale specimens were tested. As represented in Fig. 2, the

79 beam span was 3000 mm and column height was 1500 mm. Extra overhanging beam with length of
80 655 mm, connected with a roller, was extended outside the side column to simulate horizontal
81 constraints from the remaining structures of the six-story steel frame. Two types of connections are
82 tested: (1) welded connection with gross beam section (Specimen GBS) and welded connection with
83 reduced beam section RBS (Specimen RBS), as it shown in Fig. 3. For GBS, the beam flange and
84 web were welded to column flange by full penetration welds. Continuity plates with thickness of 10
85 mm were used in the column. For RBS, similar to GBS, the beam flanges and web were connected to
86 the column by same weld. However, partial of beam flanges, at a distance of 70 mm from the column
87 flange, was cut in a circular manner, as shown in Fig. 3b.

88 In both specimens, HW 150×150×7×10 and HN 200×100×5.5×8 were used for column and
89 beam, respectively. The steel used in test was Chinese Q235. The yield strength (f_y), yield strain (μ_y),
90 tensile strength (f_u), fracture strength (f_f), and total elongation (A_{gt}) of the steel in different
91 components are given in Table1.

92 2.2. Test setup and instrumentation

93 Fig. 4 gives the experimental setup and locations of instrumentations. The bottom of the side
94 column was connected to a pin support while the overhanging beam at both sides was connected to
95 an A-frame via a roller connection. The middle column at first story was removed prior to loading
96 process started. This is to simulate column removal due to accidental or incidental events. A
97 hydraulic jack (Item 1 in Fig. 4) was utilized to apply the vertical displacement at the top of middle
98 column until complete failure. A steel column together with a steel assembly was installed beneath
99 the hydraulic jack (Item 1 in Fig. 4) to prevent any undesired out-of-plane failure. The axial
100 compressive force with ratio of 0.3 to its capacity was applied at the side column by a hydraulic
101 jack (Item 4 in Fig. 4) with a self-equilibrium system. To monitor the structural behavior, extensive
102 instrumentations were installed. A load cell (Item 2 in Fig. 4) was installed below the hydraulic jack
103 (Item 1 in Fig. 4) to measure the applied concentrated load. Tension/compression load cell (Item 5 in
104 Fig. 4) was installed at each roller connection to measure the horizontal reaction force of the roller.

105 To measure the vertical and horizontal reaction forces of the pin support, a load pin (Item 6 in Fig. 4)
106 was installed at each pin support. Moreover, a series of linear variable differential transformers
107 (LVDTs) (Item 7 in Fig. 4) were installed along the beam span and column height to measure the
108 deformation shape of the beams and columns.

109 As shown in Fig. 2, 12 sections a series of strain gauges or strain rosettes were employed to
110 monitor the axial forces and bending moments of beams in detail. Moreover, the load resistance from
111 each story was also determined based on the strain gauge results.

112 **3. Experimental results**

113 As mentioned above, Specimens GBS and RBS were tested under monotonic vertical load until
114 failure. The test results were described as below, and the key results were summarized in Table 2.

115 *3.1. Load-displacement curves*

116 Fig. 5 shows the vertical load-displacement curve of GBS and RBS. At the initial loading stage,
117 the specimens were in elastic stage, and the vertical force increased more or less linearly with the
118 increase of vertical displacement.

119 For GBS, the yield load of 147.8 kN was recorded when middle column displacement (MCD)
120 reached 45 mm, which corresponded to the rotation θ of 0.015 rad. The rotation was defined as the
121 ratio of MCD to the beam span. However, yield load of RBS was 106.8 kN at an MCD of 37 mm ($\theta =$
122 **0.012 rad**). Therefore, the initial stiffness, representing the ratio of yield load to yield displacement,
123 of GBS and RBS was 3.3 kN/mm and 2.9 kN/mm, respectively. As shown in the figure, the load
124 resistance of GBS was higher than that of RBS before GBS reaching its peak load (PL) of 197.5 kN
125 corresponding to an MCD of 200 mm ($\theta = 0.067$ rad). After reaching PL, the load resistance of GBS
126 began to drop slowly due to weld fracture failure noticed near the connection of the middle column in
127 the first story. However, when MCD reached 281 mm ($\theta = 0.094$ rad), the load resisting capacity of
128 GBS began to re-ascend due to axial force developed in the second story (catenary action). The
129 ultimate deformation of GBS was 377 mm ($\theta = 0.126$ rad) and load resisting capacity at ultimate
130 deformation was 187.9 kN, which was about 95.1 % of its PL. Different to GBS, RBS kept

131 increasing until reaching its PL of 407.0 kN at an MCD of 468 mm ($\theta = 0.156$ rad). Thus, the PL and
132 ultimate deformation capacity of RBS was 106.1 % and 24.1 % higher than that of GBS, respectively.
133 The measured rotation capacity of RBS is about 201.0 % of the value determined according to FEMA
134 350 [32]. Therefore, GBS has a higher initial stiffness and load resisting capacity before the failure.
135 But pre-mature weld failure at beam-column connection would decrease deformation capacity of
136 GBS significantly. For RBS, the plastic hinges were formed at the center of the reduced beam section,
137 which would prevent the early fractures in the welding connection of the specimen.

138 3.2. Damage development and failure modes

139 For GBS, with the increase of the vertical displacement, fracture first occurred at the beam
140 flange in the region of middle column on first story (BEMC-1), as well as left beam end close to the
141 edge column on first story (LBESC-1) with MCD recorded of 200 mm ($\theta = 0.067$ rad). Then, the
142 fracture propagates into the web. At an MCD of 377 mm ($\theta = 0.126$ rad) BEMC-1 fractured, while
143 BEMC-2 fractured at the MCD of 410 mm ($\theta = 0.137$ rad). The failure mode of GBS is illustrated in
144 Fig. 6. As shown in the figure, complete fracture was observed in the left side of BEMC-2 and right
145 side of BEMC-1. However, only top flange and partial of web was fractured in LBESC-1.

146 For RBS, plastic hinges were formed at the reduced sections at an MCD of 37 mm ($\theta = 0.012$
147 rad). Due to considerable tensile axial force developed in the beams, fracture was first observed at
148 beam reduced section nearby the right side column of first story (RBESC-1) at an MCD of 468 mm
149 ($\theta = 0.156$ rad). Fig. 7 shows the failure mode of RBS. As shown in the figure, fracture only observed
150 in RBESC-1. Further increasing the displacement was prevented due to stroke of the jack reached its
151 capacity. From the figure, the peeling zone of BEMC-1 was greater than that of BEMC-2. And larger
152 plastic rotation was concentrated in BEMC-1.

153 3.3. Deformation measurements

154 The deformation shape of edge column was shown in Fig. 8. As shown in Fig. 8a, inward
155 movement was observed at the position coincide with the beam axis. However, the inward movement
156 at the position coincide with the beam axis of second story was much larger than that of first story as

157 greater catenary action developed in there. The pre-mature fracture in BEMC-1 and LBESC-1
158 prevents further developing catenary action in the beams of first story. Moreover, double curvature
159 was observed in edge column. However, the location of contra-flexural point was varying with
160 increasing MCD. The maximum inward movements of the points coincide with beam axis in the first
161 and second stories were 3.2 mm and 9.1mm, respectively. For RBS, as shown in Fig. 8b, no contra-
162 flexural point was observed in the side column due to both beams developed considerable tensile
163 force. Moreover, the maximum inward movements of the point coincide with beam axis in the first
164 and second stories were 11.6 mm and 21.0 mm, respectively.

165 Fig. 9 shows the deflection shape of the beams in the first story at different displacement stages.
166 In elastic stage, for both specimens, the deformation shape of the beams was similar to a straight line.
167 For GBS, the beam deformation in the first story was mostly concentrated on the beam end near edge
168 column rather than the middle column, thus the fracture finally developed in BEMC-1. For RBS,
169 further increasing MCD, the deformation of first story appeared on the both beam end nearby the
170 middle column and side column. Plastic hinges formed in reduced beam sections and double
171 curvature was observed.

172 *3.4. Horizontal reaction force*

173 Fig. 10a illustrates the horizontal reaction v.s. vertical displacement curve of GBS. From the
174 figure, compressive force was mainly attributed into the bottom pin support. The maximum
175 compressive force of -24.7 kN was measured at an MCD of 48 mm ($\theta = 0.016$ rad) in the bottom pin
176 support. When the MCD reached 144 mm ($\theta = 0.048$ rad), the compressive force was transferred into
177 tension. However, the tensile force from the bottom pin was always marginal in catenary action stage
178 and majority of tensile force was provided by the rollers connected to the overhanging beams in the
179 first and second stories. However, it should be noted that the maximum tensile force measured in the
180 first and second stories were 126.1 kN and 253.5 kN, respectively. This may due to pre-mature
181 failure occurred at the first story. Focusing on the total reaction force, tensile force was measured
182 when the MCD exceeded 115 mm ($\theta = 0.038$ rad). Thus, for GBS with welded connections, the

183 catenary action was mobilized at 3.8 % of the beam span. Fig. 10b illustrates the horizontal reaction
 184 force-vertical displacement curve of RBS. Similarly, the compressive reaction force was mainly
 185 attributed into the bottom pin support. However, different to GBS, in catenary action stage, the
 186 tensile force from the first and second story was almost identical. The maximum total tensile force
 187 was 875.9 kN, which was about 241.0 % of that of GBS.

188 3.5. Internal force measurements

189 **The axial force and bending moment can be calculated conveniently according to Eqs. 1 and 2.**
 190 As the middle portion of the beam kept straight during test, strain gauge results in sections B9 and
 191 B10 were utilized to determine the internal forces. Fig. 11 is the free body diagram of the beam
 192 portion between sections B10 and B9. **From basic analysis, the shear force can be calculated by Eq. 3:**

$$193 \quad N_1 = EA \left(\sum_{i=1}^n \varepsilon_i \right) / n \quad (1)$$

$$194 \quad M_1 = EI \frac{\Delta \varepsilon}{h_w} \quad (2)$$

$$195 \quad V_1 = (M_{B10} - M_{B9}) / \Delta L \quad (3)$$

196 **where N_1 , M_1 and V_1 are the axial force, bending moment and shear force of sections B9 and B10,**
 197 **respectively; E is the elastic modulus; A is the beam section area; I is the sectional moment of area;**
 198 **$\left(\sum_{i=1}^n \varepsilon_i \right) / n$ is the axial strain of section; $\Delta \varepsilon$ is the difference between the measured strains of three**
 199 **gauges at flanges (an averaged strain for each flange); h_w is the height of web; ΔL is the distance**
 200 **between sections B10 and B9.**

201 The vertical and horizontal force of the beam in the first story could be determined by Eqs. 4
 202 and 5, respectively.

$$203 \quad F_{V1} = V_1 \cos \theta_{B10} + N_1 \sin \theta_{B10} \quad (4)$$

$$204 \quad F_{H1} = V_1 \sin \theta_{B10} + N_1 \cos \theta_{B10} \quad (5)$$

205 where F_{V1} and F_{H1} are the vertical force and horizontal reaction force of a beam in the first story.
206 According to Fig. 9, the deflection between beam spanwise distance of -2250 mm and -750 mm can
207 be approximated as a straight line, θ_{B10} is the rotation at section B10 which equals to the rotation at
208 beam spanwise distance of -2250 mm.

209 The vertical force and horizontal reaction force of the beam in second story can be calculated
210 similarly. Fig. 12 compares the total vertical load resistance and total horizontal reaction force based
211 on strain gauge results with that measured from tests. As shown in Fig. 12a, for GBS, before MCD
212 reached 280 mm ($\theta = 0.093$ rad), the vertical load resistance and horizontal reaction force determined
213 based on strain gauge results agreed with the load cell measured values well. When MCD was
214 beyond 280 mm ($\theta = 0.093$ rad), the discrepancy became larger due to partial of strain gauges faulted.
215 For RBS, both vertical load resistance and horizontal reaction force determined from strain gauge
216 results agreed with the load cell measured results well. Therefore, it was reliable to use strain gauge
217 results to determine the bending moment and axial force of the beams. Moreover, based on strain
218 gauge results, the load resistance of each story could be determined.

219 Fig. 13 illustrates the variation of the total bending moment and total axial force of the
220 specimens while Fig. 14 gives the de-composition of load resistance from catenary action (CA) and
221 flexural action (FA). As shown in Fig. 13, before MCD reached 128 mm ($\theta = 0.043$ rad) and 144 mm
222 ($\theta = 0.048$ rad), bending moment and flexural action dominated the load resistance of GBS and RBS,
223 respectively. After that stage, FA and CA worked together to help redistribute the applied load. Thus,
224 it was not accurate to assume that the load resistance purely relied on CA in large deformation stage
225 [33-35].

226 4. Discussion of experimental results

227 4.1. Contribution of load resistance

228 Fig. 15 decomposes the load resistance from first and second stories. It can be seen that the load
229 resistance from the first story dropped quickly after weld fracture at the connection. Therefore, the
230 behavior of each story may be quite different due to variation of quality welding workmanship. For

231 RBS, the load resistance from each story was similar during the test. However, for both specimens,
232 the load resistance from the first story was slightly larger than that from the second story, similar
233 phenomena has been discovered by Fu [36]. To reveal the difference, the axial force and bending
234 moment results of each story were determined and presented in Fig. 16. As shown in the figure, the
235 bending moment from the first story was slightly larger than that from the second story mainly due to
236 higher rotational restraints from the side column. The axial force in the first story was always tensile
237 during the test while compressive force was measured in the second story first. This could be
238 explained as the two-story frame could be analyzed as a deep beam. The beams in the first story
239 suffered tensile force while the second story suffered compressive force when a concentrated load
240 was initially applied in the middle column.

241 *4.2. Bending moment-axial force interaction diagram*

242 Fig. 17 shows the moment and axial force interaction diagram of tested specimens. The
243 theoretical interaction diagrams of the beam section were calculated based on the measured yield and
244 ultimate strength from coupon tests (ANSI/AISC 360-10 [37]). As shown in the figure, the bending
245 moment capacity of GBS exceeded its theoretical yield capacity. However, it is less than its
246 theoretical ultimate strength. For RBS, the measured bending moment capacity is larger than its
247 theoretical ultimate strength based on reduced section. However, it is still less than the theoretical
248 ultimate strength of GBS.

249 *4.3. Practical implications from experimental results of RBS*

250 The RBS connection was designed to only resist pure bending in seismic loading according to
251 FEMA 350 [32] and ANSI/AISC 358-10 [38]. However, it will be subjected to combine bending and
252 tension when a middle column is removed. Previous works [12, 39] indicated that the current
253 acceptance criteria of rotation capacity for RBS connection are probably too conservative. Plastic
254 hinge formed in RBS connection would help to enhance its rotation capacity and enable full
255 development of tying capacity. Thus, it was necessary to develop a calculation model for quantify
256 the tying capacity of RBS connections.

257 According to Chapter H of ANSI/AISC 360-10 [37], the required axial strength P_r were
 258 corrected owing to the presence of the bending moment. The tying capacity of RBS connection can
 259 be determined by Eq. 6:

$$260 \quad \begin{cases} P_r \leq P_c \left[1.0 - \frac{8}{9} \left(\frac{M_{rx}}{M_{cx}} + \frac{M_{ry}}{M_{cy}} \right) \right], & \text{when } P_r \geq 0.2P_c \\ P_r \leq 2P_c \left[1.0 - \left(\frac{M_{rx}}{M_{cx}} + \frac{M_{ry}}{M_{cy}} \right) \right], & \text{when } P_r < 0.2P_c \end{cases} \quad (6)$$

261 where P_c is the available axial strength, M_r and M_c are the required and available flexural
 262 strength, and x and y are the subscript to represent strong axis and weak axis, respectively.

263 As the tensile force dominated the behavior and failure mode of RBS at large deformation stage,
 264 Yang and Tan [16] proposed the tying resistance of the connections equal to the contribution of CA.

265 Thus, the tying resistance P_r' of RBS connection can be described as followed:

$$266 \quad P_r' = P_r \sin \theta_c \quad (7)$$

267 where θ_c is the rotation capacity of RBS connections.

268 The probable maximum moment at the center of reduced beam section specified in FEMA 350
 269 [32] is evaluated based on the yield capacity. As mentioned above, the capacity of RBS exceeded the
 270 ultimate capacity of RBS under combined axial and flexural loads. Similar observation was
 271 concluded by Sadek et al. [40]. This implies that the acceptance criteria give a low-bound estimation
 272 for RBS connection.

273 5. Numerical analysis

274 5.1. Numerical model

275 To further investigate the behavior of steel sub-frames with RBS against progressive collapse,
 276 FE models using explicit software LS-DYNA [41] were employed due to its numerical stability and
 277 variety of constitutive models [42-50]. Many other software has been used in progressive collapse
 278 analysis [51], however, it is found that LS-DYNA is one of the most powerful software. Therefore, it
 279 is used here. The FE models were validated by comparing with experimental results. As shown in Fig.

280 18a, boundary conditions applied on the FE models replicates that from the experimental tests. Due
281 to the complication in simulation of horizontal constraints (inevitable gaps exists in rollers), springs
282 was used to simulate the horizontal constraints at the overhanging beams, as shown in Fig. 18b. The
283 stiffness of the springs was determined based on the measured horizontal reaction force of the roller
284 and lateral displacements, as shown in Table 3. A vertical displacement was applied at the middle
285 column. In order to avoid dynamic vibration due to step force, smooth step amplitude displacement
286 control was used. Further, the ratio of the kinetic energy and external work was maintained less than
287 1 % [39].

288 Fig. 18b shows the FE model of the specimen. The beam/columns were simulated by 8-node
289 solid elements with a reduced integration, but the springs used discrete elements. As numerical
290 results are sensitive to the material properties, adopting appropriate constitutive model is crucial.
291 Within the material library of LS-DYNA, an isotropic elastic-plastic material model
292 *Mat_Piecewise_Linear_Plasticity (MAT_024) was used for steel. The measurements showed that
293 the deviations from the nominal geometries of the two specimens were very small. The FE models
294 were created using the nominal values. The material properties were defined based on measured
295 material property (see Table 1). Pin supports were simulated by using the keyword
296 *CONSTRAINED_JOINT_REVOLUTE (see Fig. 18b).

297 Fig .19 shows the mesh of the joint zone with different sizes. For Mesh 1, 10 mm was meshed in
298 the potential plastic hinge zone while remaining parts were meshed with size of 30 mm. For Mesh 2
299 and 3, the remaining parts were meshed with size of 20 mm and 10 mm, respectively. As shown in
300 Fig. 20a, there was no big difference for Mesh 1, 2, and 3 in terms of initial stiffness, peak load, and
301 deformation capacity. Therefore, Mesh 1 was selected in this numerical study due to computational
302 cost consideration.

303 5.2. *Verification of numerical model*

304 Figs. 20-21 show the comparison of the experimental and numerical results. In generally, the
305 numerical models agree well with the experimental results in terms of vertical load resistance,

306 horizontal reaction force, and axial force in beams. Figs. 22 and 23 show the simulated failure mode
307 of GBS and RBS, respectively. Comparing with test results, the fracture of the connection and plastic
308 deformation of the connections were well simulated. Thus, it was reliable to adopt the validated FE
309 models for further parametric study.

310 **6. Parametric study**

311 Based on the validated models, the effects of span/depth ratio and other section reduction
312 method on behavior of steel frames to resist progressive collapse were quantified.

313 *6.1. Span/depth ratio*

314 Fig. 24 illustrates the influence of different span/depth ratio k on load resistance of RBS. where
315 $k = L/d_{beam}$, L represents the beam span and d_{beam} represents the height of beam. Moreover, d_{beam}
316 keeps constant and beam span increases with increase of the span/depth ratio. As shown in the figure,
317 when k decreased from 15 to 10, the PL increased by 12.1 % and the ultimate deformation capacity
318 decreased by 31.0 %. However, when k increased from 15 to 22.5 and 30, the deformation capacity
319 increased by 56.3 % and 102.3 %, respectively. However, the PL decreased by 3.3 % and 0.8 %,
320 respectively. The deformation capacity of the specimen decreases with decrease of the span/depth
321 ratio. However, it will not affect the PL significantly as PL was mainly controlled by catenary action.
322 If the MCD was replaced by rotation, which was defined as the ratio of MCD to beam span, the
323 span/depth ratio will affect the initial stiffness of the steel frame significantly. However, it will not
324 affect the rotation capacity significantly, as shown in Fig. 24b.

325 *6.2. Different section reduction methods*

326 To investigate the collapse behavior of the welded connection with reduced beam section (i.e.
327 reduced beam section) further, four reduction types are investigated (refer to Fig. 25). Morshedi et al.
328 [52] provided a reference for the design of the double reduced beam section (DRBS) (refer to Fig.
329 25a). Opening in beam flange (OBW) (refer to Fig. 25b) is proposed by Chung et al. [53] as an
330 effective method to improve the behavior of steel frame to resist progressive collapse. Meng [54]
331 suggested an innovative method to punch an opening in beam flange (OBF) (refer to Figs. 25c and

332 25d), where OBF-2 and OBF-3 represent two and three holes in beam flange, respectively. However,
333 the total opening area of OBF-2 and OBF-3 was identical.

334 6.2.1. Double reduced beam section

335 Fig. 26a compares the load resistance of RBS and DRBS. As can be seen from the figure, the
336 curves almost coincide before the MCD of 36 mm ($\theta = 0.012$ rad) in elastic stage. Similar to RBS,
337 with increasing the vertical displacement, plastic hinges were formed at the position of reduced
338 sections in DRBS. Actually, before fracture occurred in the beam of RBS, these two curves are
339 similar. The PL of RBS and DRBS were 394.8 kN and 544.2 kN, respectively. The ultimate
340 deformation capacity of RBS and DRBS were 435 mm ($\theta = 0.145$ rad) and 529 mm ($\theta = 0.176$ rad),
341 respectively. Thus, DRBS could increase the PL and deformation capacity by 37.9 % and 21.5 %,
342 respectively. The failure mode of DRBS is shown in Fig. 27.

343 6.2.2. Perforated beam section

344 OBW, OBF-2 and OBF-3 are perforated openings with same total opening area at the web or
345 flanges base on the validated FE model of GBS. Fig. 26b compares the load resistance of GBS,
346 OBW, OBF-2, and OBF-3. As can be seen from the figure, OBW achieved the highest PL and
347 deformation capacity in these perforated beam section specimens. When MCD reached 30 mm ($\theta =$
348 0.010 rad), plastic hinges concentrated in the perforated zone of the web and propagates rapidly. At
349 MCD of 415 mm ($\theta = 0.138$ rad) corresponding load resistance of 225.0 kN, BEMC-1 fractured at
350 the bottom flange. At MCD of 500 mm ($\theta = 0.167$ rad) and 550 mm ($\theta = 0.183$ rad), bottom flanges
351 in BEMC-1 and BEMC-2 completely fractured one by one. However, the load resistance did not
352 decrease until the fracture propagated into the top flange and completely detached at MCD of 600
353 mm ($\theta = 0.200$ rad). The failure mode of OBW is shown in Fig. 28. Completely fracture occurred in
354 the center of opening of the beam web. Compared with GBS, the PL and deformation capacity of
355 OBW was increased by 20.9 % and 76.5 %, respectively.

356 As shown in Fig. 26b, compared with GBS, the deformation capacity of OBF-2 and OBF-3
357 were increased by 44.8 % and 62.4 % respectively. However, the PL of OBF-2 and OBF-3 were only

358 about 58.4 % and 79.6 % of that of GBS. Therefore, punching opening in the flange of the beam
359 section will decrease the load resistance but increase the deformation capacity. OBF-3 performed
360 much better than that of OBF-2 mainly due to larger opening size in OBF-2 although total opening
361 area was same in these two models. The failure modes of OBW-2 and OBW-3 are shown in Figs. 29
362 and 30. The fracture of OBW-2 and OBW-3 first occurred in the perforated beam section of the
363 flange.

364 **7. Conclusions**

365 The experimental investigations under a middle column removal scenario were carried out to
366 study the behavior of steel substructures with welded connection with seismic configurations. Based
367 on experimental results, detailed FE models were established to conduct parametric study using finite
368 element software LS-DYNA. The following conclusions are drawn:

- 369 1. The experimental results indicated that the performance of welded connection with RBS was
370 superior to the welded connection with GBS. The resistance and deformation capacity of RBS
371 was 106.1 % and 24.1 % higher than that of GBS.
- 372 2. At the initial stage of column removal, the beams in different stories deform together. Thus, the
373 beams in the first story suffered tension while the beams in the second story experienced
374 compression. Looking at the load resistance, in relatively small deformation stage, the load
375 resistance from the beams in the first story is higher than that of the beams in the second story.
376 However, in large deformation stage, the load resistance of these two stories is similar for RBS.
377 For GBS, the load resistance of the beams in the first story is much less than that from second
378 story in large deformation stage may be due to undesired pre-mature fracture at the welding
379 connection of the first story.
- 380 3. Experimental results indicated that flexural action and catenary action worked together to resist
381 progressive collapse of the frame in large deformation stage. It was confirmed that measured
382 rotation capacity of steel frames with welded connections, especially with reduced beam section,
383 is much larger than the value predicted based on design code FEMA 350 [32].

- 384 4. Analytical results indicated that the measured bending moment capacity of critical section could
385 exceed the yield bending moment capacity due to bending moment-tension composite action.
- 386 5. Numerical and parametric studies indicated that the deformation capacity of steel frames increase
387 as the span-depth ratio increase. However, span-depth ratio has little effects on ultimate rotation
388 capacity and ultimate load. Double reduced beam section could further upgrade the load resisting
389 capacity and deformation capacity of the steel frames. Punched openings in the beam flange will
390 decrease the initial stiffness and load resistance but increase the deformation capacity
391 significantly.
- 392 6. Catenary action contributes to arrest progressive collapse of steel structures at large deformation
393 stage, therefore, sufficient deformation capacity of the connection should be designed. This
394 implies that engineers could adopt effective section reduction methods to motivate catenary
395 action of the steel frames adequately, but it should be taken in moderation due to the decrease of
396 its load resisting capacity.

397 **Acknowledgements**

398 This research was supported by a research grant provided by the Natural Science Foundation of
399 China (Nos.51778153, 51568004), and Guangxi university postgraduate education innovation
400 program (No. YCBZ2019024). Any opinions, findings and conclusions expressed in this paper do not
401 necessarily reflect the view of Natural Science Foundation of China.

402 **Future work**

403 As the next steps in this research program, we intend to perform more experimental study taking
404 into consideration infilled wall with the steel moment frames under the middle column removal
405 scenario.

406 **References**

- 407
- 408 [1] C. Málaga-Chuquitaype, A.Y. Elghazouli, R. Enache, Contribution of secondary frames to the
409 mitigation of collapse in steel buildings subjected to extreme loads, *Struct. Infrastruct. Eng.* 12(1)
410 (2016) 45-60.

- 411 [2] E. Stoddart, M. Byfield, B. Davison, A. Tyas, Strain rate dependent component based connection
412 modelling for use in non-linear dynamic progressive collapse analysis, *Eng. Struct.* 55 (2013) 35-
413 43.
- 414 [3] O.A. Mohamed, Calculation of load increase factors for assessment of progressive collapse
415 potential in framed steel structures, *Case Stud. Struct. Eng.* 3 (2015) 11-18.
- 416 [4] J.J. Mashhadi, H. Saffari, Dynamic increase factor based on residual strength to assess
417 progressive collapse, *Steel Comp. Struct.* 25(5) (2017) 617-624.
- 418 [5] A. McKay, K. Marchand, M. Diaz, Alternate path method in progressive collapse analysis:
419 variation of dynamic and nonlinear load increase factors. *Practice periodical on structural design
420 and construction, Pract. Period. Struct. Des. Constr.* 17(4) (2012) 152-160.
- 421 [6] M. Liu, A new dynamic increase factor for nonlinear static alternate path analysis of building
422 frames against progressive collapse, *Eng. Struct.* 48 (2013) 666-673.
- 423 [7] M. Ferraioli, Dynamic increase factor for pushdown analysis of seismically designed steel
424 moment-resisting frames, *Int. J. Steel Struct.* 16(3) (2016) 857-875.
- 425 [8] M. Ferraioli, A. Lavino, A. Mandara, Dynamic increase factor for nonlinear static alternate path
426 analysis of steel moment-resisting frames against progressive collapse, *ce/papers* (2017).
- 427 [9] M. Ferraioli, A modal pushdown procedure for progressive collapse analysis of steel frame
428 structures, *J. Constr. Steel Res.* 156 (2019) 227-241.
- 429 [10] T. Kim, J. Kim, J. Park, Investigation of progressive collapse-resisting capability of steel
430 moment frames using push-down analysis, *J. Perform. Constr. Facil.* 23(5) (2009) 327-335.
- 431 [11] M. Ferraioli, Evaluation of dynamic increase factor in progressive collapse analysis of steel
432 frame structures considering catenary action, *Steel Comp. Struct.* 30(3) (2019) 253-269.
- 433 [12] H.S. Lew, J.A. Main, S.D. Robert, et al., Performance of steel moment connections under a
434 column removal scenario. I: Experiments, *J. Struct. Eng.* 139 (1) (2013) 98-107.
- 435 [13] W.H. Zhong, B. Meng, J.P. Hao, Performance of different stiffness connections against
436 progressive collapse, *J. Constr. Steel Res.* 135 (2017) 162-175.

- 437 [14] B. Meng, W.H. Zhong, J.P. Hao, Anti-collapse performances of steel beam-to-column
438 assemblies with different span ratios, *J. Constr. Steel Res.* 140 (2018) 125-138.
- 439 [15] M. Xu, S. Gao, L.H. Guo, et al., Study on collapse mechanism of steel frame with CFST-
440 columns under column-removal scenario, *J. Constr. Steel Res.* 141 (2018) 275-286.
- 441 [16] B. Yang, K.H. Tan, Experimental tests of different types of bolted steel beam-column joints
442 under a central-column-removal scenario, *Eng. Struct.* 54 (2013) 112-130.
- 443 [17] L. Li, W. Wang, Y.Y. Chen, Y. Lu, Experimental investigation of beam-to-tubular column
444 moment connections under column removal scenario, *J. Constr. Steel Res.* 88 (2013) 244-255.
- 445 [18] L. Li, W. Wang, Y.Y. Chen, Y. Lu, Effect of beam web bolt arrangement on catenary behaviour
446 of moment connections, *J. Constr. Steel Res.* 104 (2015) 22-36.
- 447 [19] M. Xu, S. Gao, S.M. Zhang, H.H. Li, Experimental study on bolted CFST-column joints with
448 different configurations in accommodating column-loss, *J. Constr. Steel Res.* 151 (2018) 122-
449 131.
- 450 [20] S. Gao, M. Xu, F. Fu, L.H. Guo, Performance of bolted steel-beam to CFST-column joints using
451 stiffened angles in column-removal scenario, *J. Constr. Steel Res.* 159 (2019) 459-475.
- 452 [21] L.H. Guo, S. Gao, F. Fu, Y.Y. Wang, Experimental study and numerical analysis of progressive
453 collapse resistance of composite frames, *J. Constr. Steel Res.* 89 (2013) 236-251.
- 454 [22] B. Yang, K.H. Tan, G. Xiong, S.D. Nie, Experimental study about composite frames under an
455 internal column-removal scenario, *J. Constr. Steel Res.* 121 (2016) 341-351.
- 456 [23] S.B. Kang, K.H. Tan, H.Y. Liu, et al., Effect of boundary conditions on the behaviour of
457 composite frames against progressive collapse, *J. Constr. Steel Res.* 138 (2017) 150-167.
- 458 [24] S. Gao, L.H. Guo, F. Fu, S.M. Zhang, Capacity of semi-rigid composite joints in accommodating
459 column loss, *J. Constr. Steel Res.* 139 (2017) 288-301.
- 460 [25] R. Zandonini, N. Baldassino, F. Freddi, G. Roverso, Steel-concrete frames under the column loss
461 scenario: An experimental study, *J. Constr. Steel Res.* 162 (2019) UNSP 105527.
- 462 [26] G.C. Zhou, J. Shi, P.C. Li, H.H. Li, Characteristics of structural state of stress for steel frame in
463 progressive collapse, *J. Constr. Steel Res.* 160 (2019) 444-456.

- 464 [27] J.J. Wang, W. Wang, Y.H. Bao, D. Lehman, Full-scale test of a steel moment-resisting frame
465 with composite floor under a penultimate edge column removal scenario, *J. Constr. Steel Res.*
466 162 (2019) UNSP 105717.
- 467 [28] J.J. Wang, W. Wang, D. Lehman, C. Roeder, Effects of different steel-concrete composite slabs
468 on rigid steel beam-column connection under a column removal scenario, *J. Constr. Steel Res.*
469 153 (2019) 55-70.
- 470 [29] G.Q. Li, L.L. Li, B.H. Jiang, Y. Lu, Experimental study on progressive collapse resistance of
471 steel frames under a sudden column removal scenario, *J. Constr. Steel Res.* 147 (2018) 1-15.
- 472 [30] L.L. Li, G.Q. Li, B.H. Jiang, Y. Lu, Analysis of robustness of steel frames against progressive
473 collapse, *J. Constr. Steel Res.* 143 (2018) 264-278.
- 474 [31] American Institute of Steel Construction, *Seismic Provisions for Structural Steel Buildings.*
475 *ANSI/AISC 341-10*, Chicago, USA 2010.
- 476 [32] Federal Emergency Management Agency, *Recommended Seismic Design Criteria for New Steel*
477 *Moment-Frame Buildings. FEMA 350*, Washington (DC), USA 2000.
- 478 [33] H.H. Li, X.H. Cai, L. Zhang, et al., Progressive collapse of steel moment-resisting frame
479 subjected to loss of interior column: Experimental tests, *Eng. Struct.* 150 (2017) 203-220.
- 480 [34] B. Yang, K.H. Tan, Numerical analyses of steel beam-column joints subjected to catenary action,
481 *J. Constr. Steel Res.* 70 (2012) 1-11.
- 482 [35] B. Yang, K.H. Tan, G. Xiong, Behaviour of composite beam-column joints under a middle-
483 column-removal scenario: Component-based modelling, *J. Constr. Steel Res.* 104 (2015) 137-
484 154.
- 485 [36] F. Fu, Progressive collapse analysis of high-rise building with 3-D finite element modeling
486 method, *J. Constr. Steel Res.* 65 (6) (2009) 1269–1278.
- 487 [37] American Institute of Steel Construction, *Specification for Structural Steel Buildings.*
488 *ANSI/AISC 360-10*, Chicago, USA 2010.
- 489 [38] American Institute of Steel Construction, *Prequalified Connections for Special and Intermediate*
490 *Steel Moment Frames for Seismic Applications. ANSI/AISC 358-10*, Chicago, USA 2010.

- 491 [39] F. Dinu, I. Marginean, D. Dubina, Experimental testing and numerical modelling of steel
492 moment-frame connections under column loss, *Eng. Struct.* 151 (2017) 861-878.
- 493 [40] F. Sadek, J.A. Main, H.S. Lew, S. El-Tawil, Performance of steel moment connections under a
494 column removal scenario. II: Analysis, *J. Struct. Eng.* 139 (1) (2013) 108-119.
- 495 [41] J. Hallquist, LS-DYNA keyword user's manual, Version 971, Livermore Software Technology
496 Corp., Livermore, CA, 2007.
- 497 [42] M. Yu, X.X. Zha, J.Q. Ye, The influence of joints and composite floor slabs on effective tying of
498 steel structures in preventing progressive collapse, *J. Constr. Steel Res.* 66 (2010) 442-451.
- 499 [43] C.G. Tay, C.G. Koh, J.Y.R. Liew, Efficient progressive collapse analysis for robustness
500 evaluation of buildings experiencing column removal, *J. Constr. Steel Res.* 122 (2016) 395-408.
- 501 [44] H. Wang, B. Yang, X.H. Zhou, S.B. Kang, Numerical analyses on steel beams with fin-plate
502 connections subjected to impact loads, *J. Constr. Steel Res.* 124 (2016) 101-112.
- 503 [45] Y. Ding, X.R. Song, H.T. Zhu, S.B. Kang, Probabilistic progressive collapse analysis of steel-
504 concrete composite floor systems, *J. Constr. Steel Res.* 129 (2017) 129-140.
- 505 [46] B. Yang, H. Wang, Y. Yang, et al., Numerical study of rigid steel beam-column joints under
506 impact loading, *J. Constr. Steel Res.* 147 (2018) 62-73.
- 507 [47] S.C. Lin, B. Yang, S.B. Kang, S.Q. Xu, A new method for progressive collapse analysis of steel
508 frames, *J. Constr. Steel Res.* 153 (2019) 71-84.
- 509 [48] X. F. Deng, S. L. Liang, F. Fu, K. Qian, Effects of high-strength concrete on progressive collapse
510 resistance of reinforced concrete frame. *Journal of Structural Engineering.* 146(6)
511 (2020)04020078.
- 512 [49] K. Qian, S. L. Liang, X. Y. Xiong, F. Fu, Q. Fang, Quasi-static and dynamic behavior of precast
513 concrete frames with high performance dry connections subjected to loss of a penultimate
514 column scenario. *Engineering Structures.* 205(2020) 110115.
- 515 [50] Y. H. Weng, K. Qian, F. Fu, Q. Fang. Numerical investigation on load redistribution capacity of
516 flat slab substructures to resist progressive collapse, *Journal of Building Engineering.* 29(2020),
517 101109.

- 518 [51] Fu, F.(2016) Structural Analysis and Design to Prevent Disproportionate Collapse. CRC Press.
 519 ISBN 978-1-4987-8820-5
- 520 [52] M.A. Morshedi, K.M. Dolatshahi, S. Maleki. Double reduced beam section connection, J.
 521 Constr. Steel Res. 138 (2017) 283-297.
- 522 [53] K.F. Chung, T.C.H. Liu, A.C.H. Ko, Investigation on Vierendeel mechanism in steel beams with
 523 circular web openings, J. Constr. Steel Res. 57 (5) (2001) 467-490.
- 524 [54] Q.X. Meng, Research on seismic behavior of beam-to-column joint with beam flange openings,
 525 Hebei University of Engineering 2017 (in Chinese).

526
 527 **Table 1-Material properties from coupon test of the connection**

Element	t (mm)	f_y (MPa)	μ_y	f_u (MPa)	f_f (MPa)	A_{gt} (%)
Beam flange	8.0	310	0.0019	420	315	12.0
Beam web	5.5	320	0.0021	430	340	13.5
Column flange	10.0	300	0.0019	410	300	14.0
Column web	7.0	295	0.0023	375	265	13.0

528 Note : t = plate thickness; f_y = yield strength; μ_y = yield stain; f_u = tensile strength; f_f = fracture strength (engineering stress); A_{gt} = total elongation at
 529 maximum stress.
 530
 531
 532

533 **Table 2-Test results**

Specimen identifier	u_{YL} (mm)	θ_{YL} (rad)	F_{YL} (kN)	K_{YL} ($\times 10^3$ kN/m)	u_{PL} (mm)	θ_{PL} (rad)	F_{PL} (kN)	M_{max} (kN·m)	N_{max} (kN)
GBS	45	0.015	147.8	3.3	200	0.067	197.5	463.1	661.9
RBS	37	0.012	106.8	2.9	468	0.156	407.0	382.7	1712.4

534 Note: F_{YL} and F_{PL} = yield load and peak load capacity; u_{YL} and u_{PL} = displacements corresponding the yield load and peak load; K_{YL} = stiffness
 535 corresponding the yield load; θ_{YL} and θ_{PL} = chord rotation corresponding the yield and peak load; M_{max} and N_{max} = maximum bending moment and
 536 maximum axial force.
 537
 538
 539

540 **Table 3-Stiffness horizontal restraints**

Element	Horizontal restraints	Stiffness ($\times 10^3$ N/mm)	Gap (mm)
GBS	1st story	46.4	0.5
	2nd story	51.0	4.1
RBS	1st story	39.2	0.7
	2nd story	31.0	0.9

541

542

543

544

545

546

547 **List of Figures**

548

549 **Fig. 1** Location of the extracted frame in the prototype building (unit in mm): (a) plan view; (b)
550 elevation view

551 **Fig. 2** Dimensions of the specimen and locations of strain gauge and displacement transducers (unit
552 in mm)

553 **Fig. 3** Details of test specimens (unit in mm): (a) GBS; (b) RBS

554 **Fig. 4** Test setup

555 **Fig. 5** Comparison of the load-displacement curves

556 **Fig. 6** Failure mode of GBS

557 **Fig. 7** Failure mode of RBS

558 **Fig. 8** Horizontal movement of the side column: (a) GBS; (b) RBS

559 **Fig. 9** Overall deflection profile of the beams in the first story: (a) GBS; (b) RBS

560 **Fig. 10** Horizontal reaction force-middle column displacement curves: (a) GBS; (b) RBS

561 **Fig. 11** Internal forces at section B10 and B9

562 **Fig. 12** Comparisons of vertical load resistance and horizontal reaction force from strain gauge and
563 load cells (a) GBS; (b) RBS

564 **Fig. 13** Variation of total bending moment and axial force of GBS and RBS

565 **Fig. 14** De-composition of the load resistance from different actions: (a) GBS (b) RBS (Note: FA and
566 CA represent flexural action and catenary action, respectively)

567 **Fig. 15** De-composition of load resistance from 1st story and 2nd story: (a) GBS; (b) RBS

568 **Fig. 16** Comparisons of the bending moment and axial force variation in 1st story and 2nd stories: (a)
569 GBS; (b) RBS

570 **Fig. 17** Bending moment-axial force interaction diagram

571 **Fig. 18** Geometric model with boundary conditions: (a) overall view; (b) zone-in view

572 **Fig. 19** Mesh configuration for different mesh strategy

573 **Fig. 20** Comparison of experimental and numerical results of GBS: (a) vertical force; (b) horizontal
574 reaction force; (c) axial force in beams

575 **Fig. 21** Comparison of experimental and numerical results of RBS: (a) vertical force; (b) horizontal
576 reaction force; (c) axial force in beams

577 **Fig. 22** Comparison of the failure mode of GBS from test and numerical model

578 **Fig. 23** Comparison of the failure mode of RBS from test and numerical model

579 **Fig. 24** Investigation on effects of span-depth ratio (k): (a) vertical force vs. MCD; (b) vertical force
580 vs. rotation

581 **Fig. 25** Details of different types of reduced beam section (unit in mm): (a) DRBS; (b) OBW; (c)
582 OBF-2; (d) OBF-3

583 **Fig. 26** Comparison of the load-displacement response: (a) RBS and DRBS; (b) GBS, OBW, OBF-2,
584 and OBF-3

585 **Fig. 27** Failure mode of DRBS: (a) overall view; (b) zone-in view

586 **Fig. 28** Failure mode of OBW: (a) overall view; (b) zone-in view

587 **Fig. 29** Failure mode of OBF-2: (a) overall view; (b) zone-in view

588 **Fig. 30** Failure mode of OBF-3: (a) overall view; (b) zone-in view

589

590

591

592

593

594

595

596

597

598

599

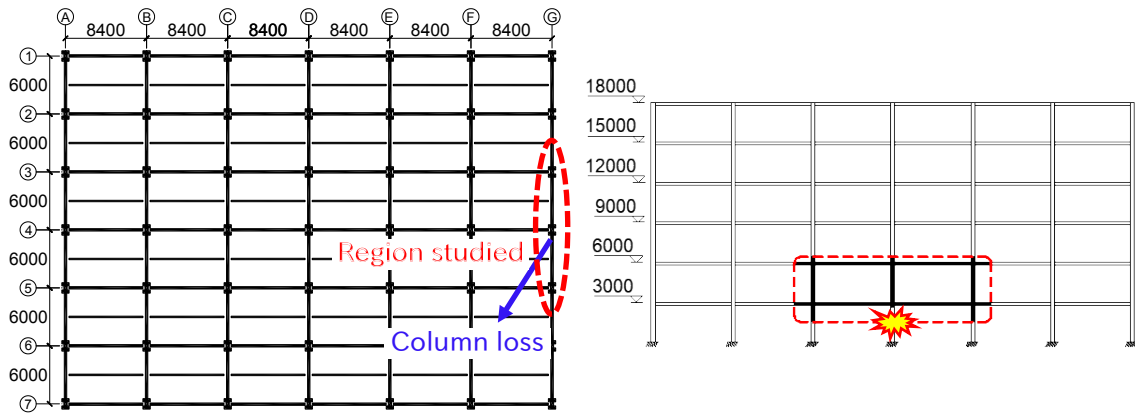
600

601

602

603

604



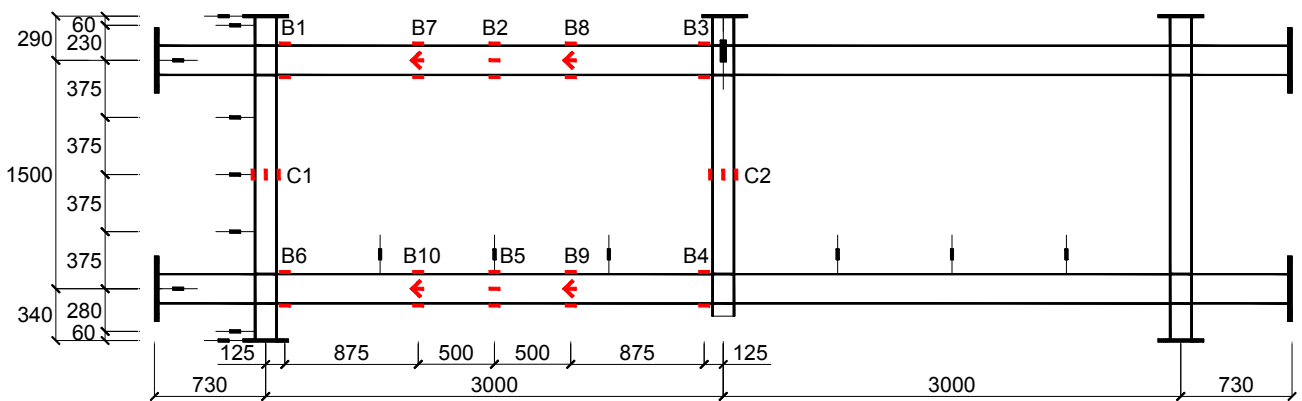
605

606

607 **Fig. 1** Location of the extracted frame in the prototype building (unit in mm): (a) plan view; (b)
608 elevation view

609

610

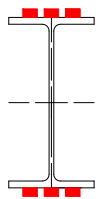


611

612

613

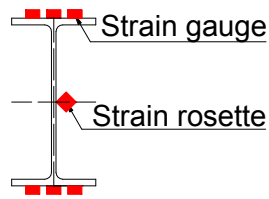
(a) Arrangements of strain gauges/rosettes and displacement transducers



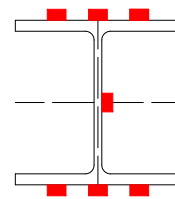
614

615

(b) Section B1 to B6



(c) Section B7 to B10



(d) Section C1 and C2

616 **Fig. 2** Dimensions of the specimen and locations of strain gauge and displacement transducers (unit
617 in mm)

618

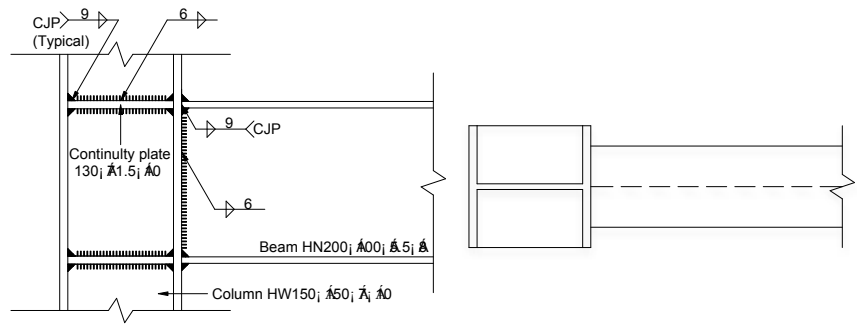
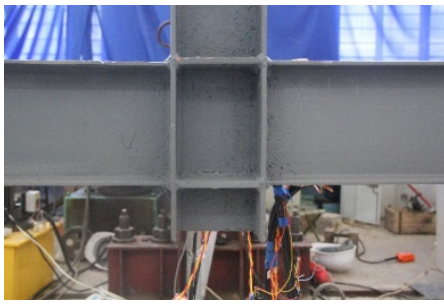
619

620

621

622

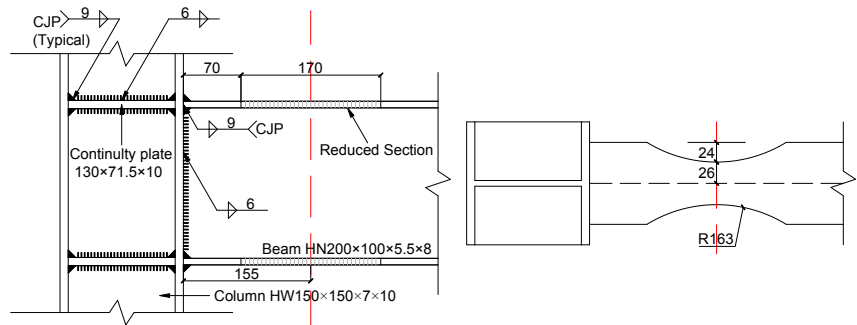
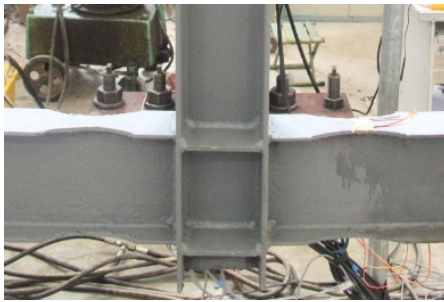
623



624

625

(a)



(b)

Fig. 3 Details of test specimens (unit in mm): (a) GBS; (b) RBS

626

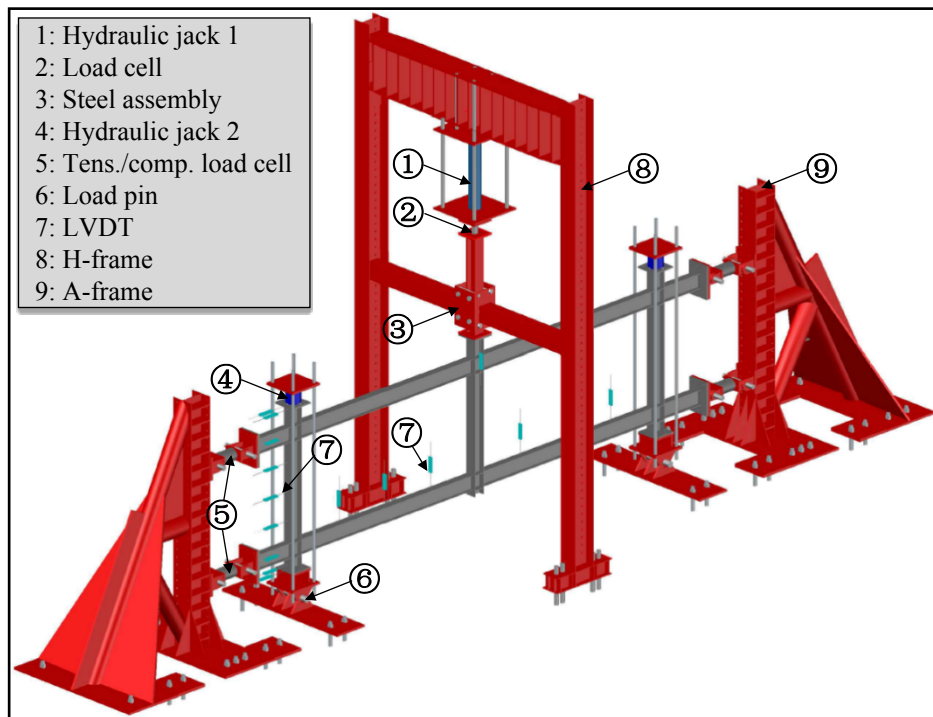
627

628

629

630

631



- 1: Hydraulic jack 1
- 2: Load cell
- 3: Steel assembly
- 4: Hydraulic jack 2
- 5: Tens./comp. load cell
- 6: Load pin
- 7: LVDT
- 8: H-frame
- 9: A-frame

632

633

634

635

Fig. 4 Test setup

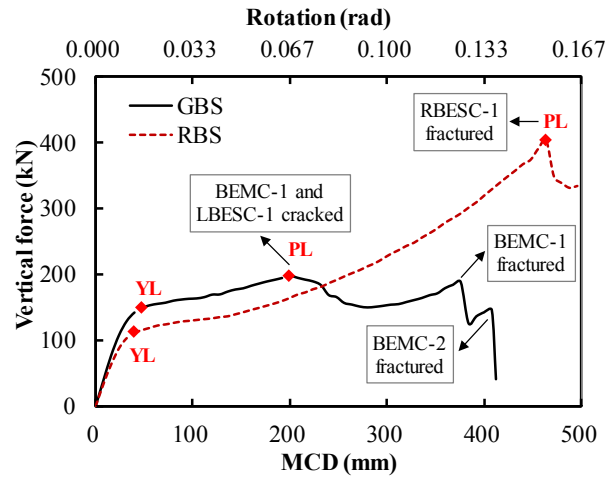


Fig. 5 Comparison of the load-displacement curves

637

638

639

640

641

642

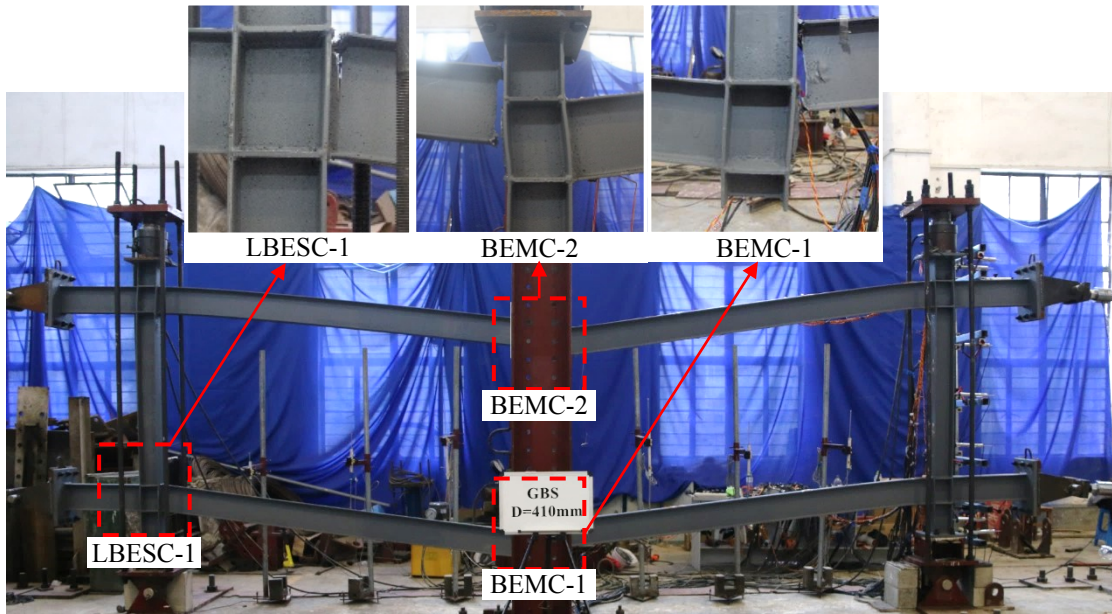


Fig. 6 Failure mode of GBS

643

644

645

646

647

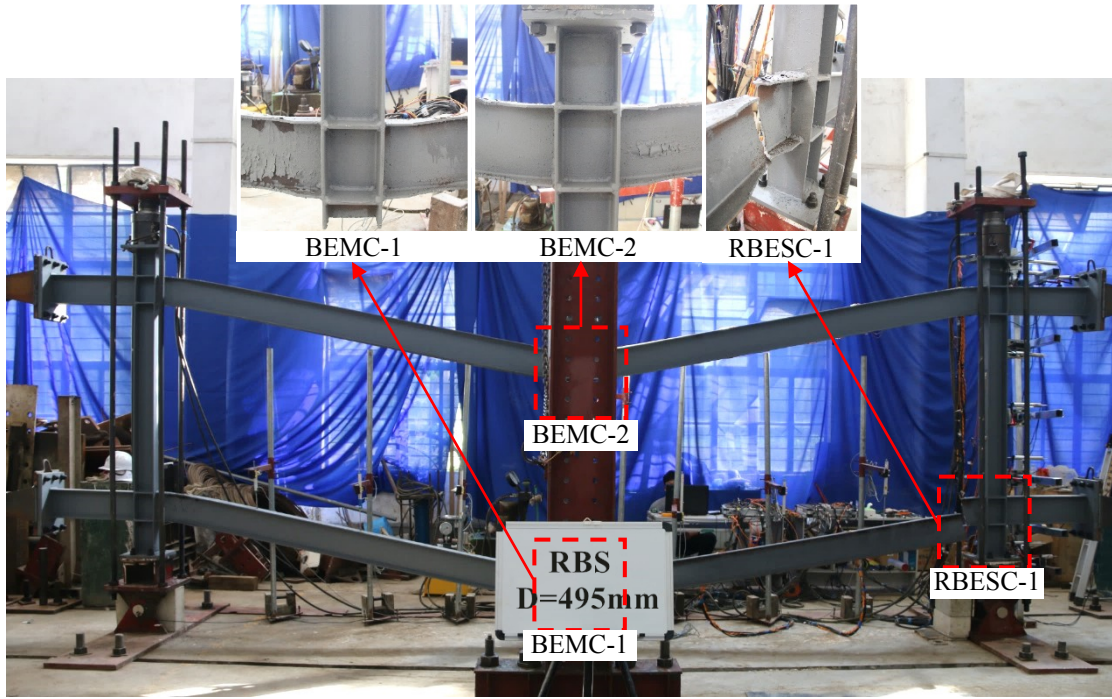


Fig. 7 Failure mode of RBS

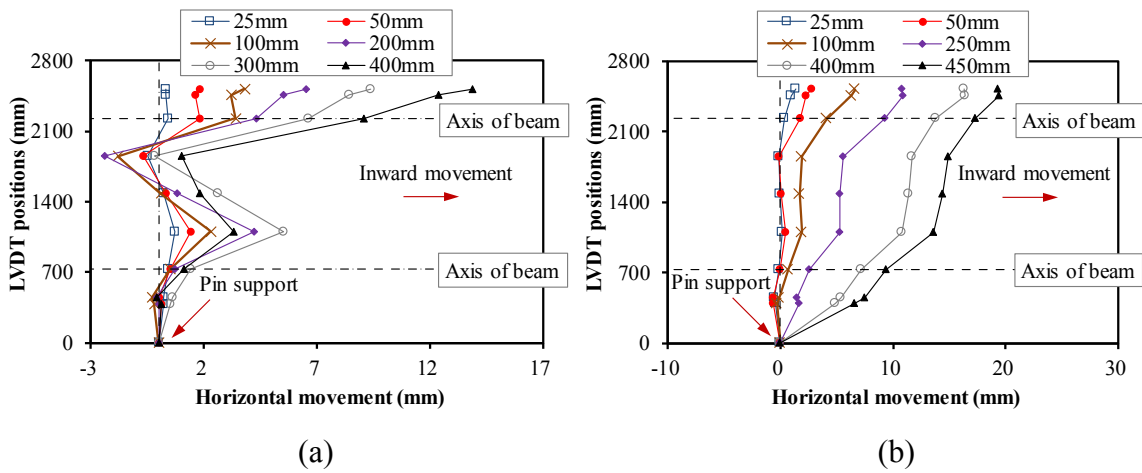
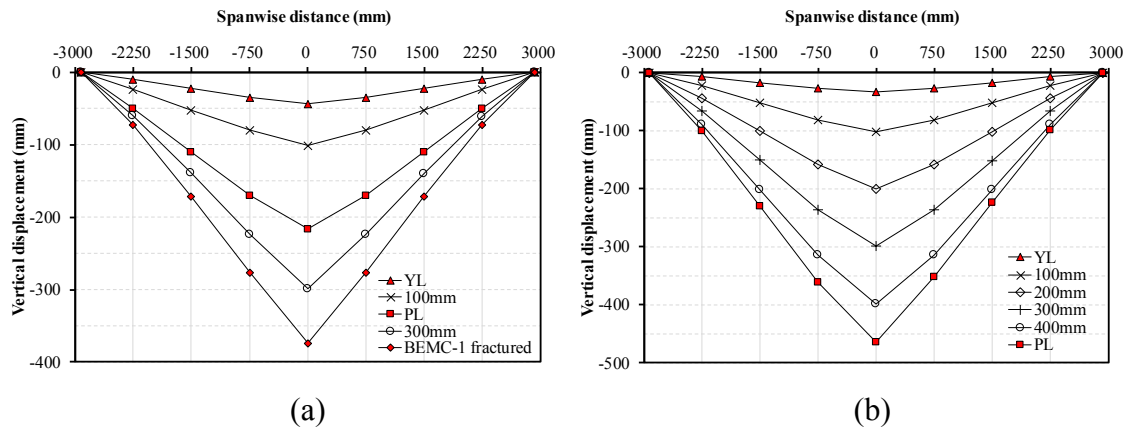
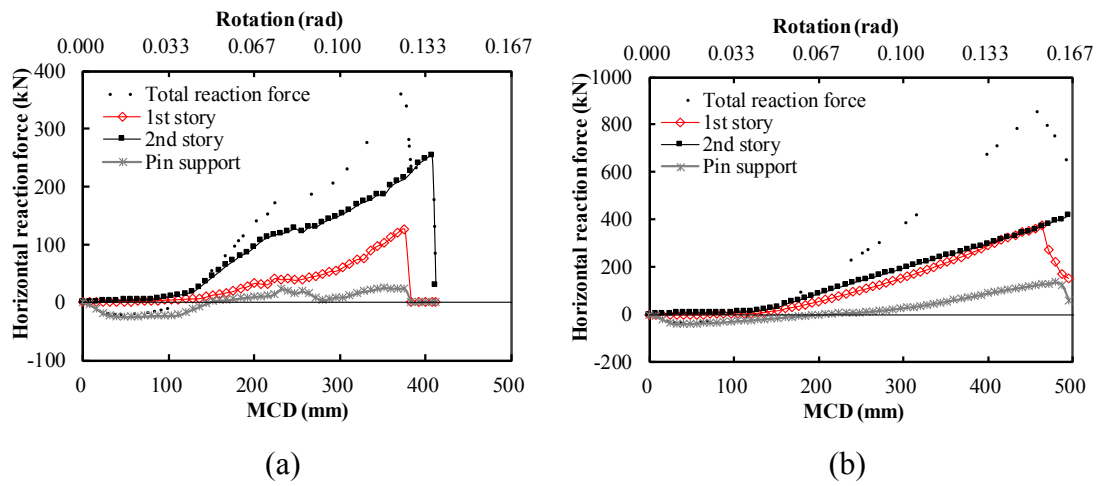


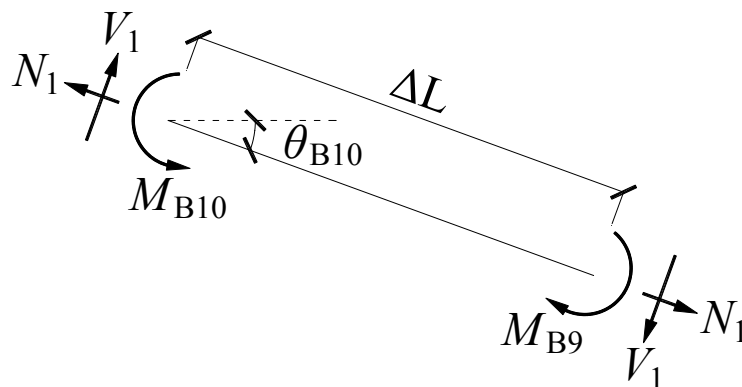
Fig. 8 Horizontal movement of the side column: (a) GBS; (b) RBS



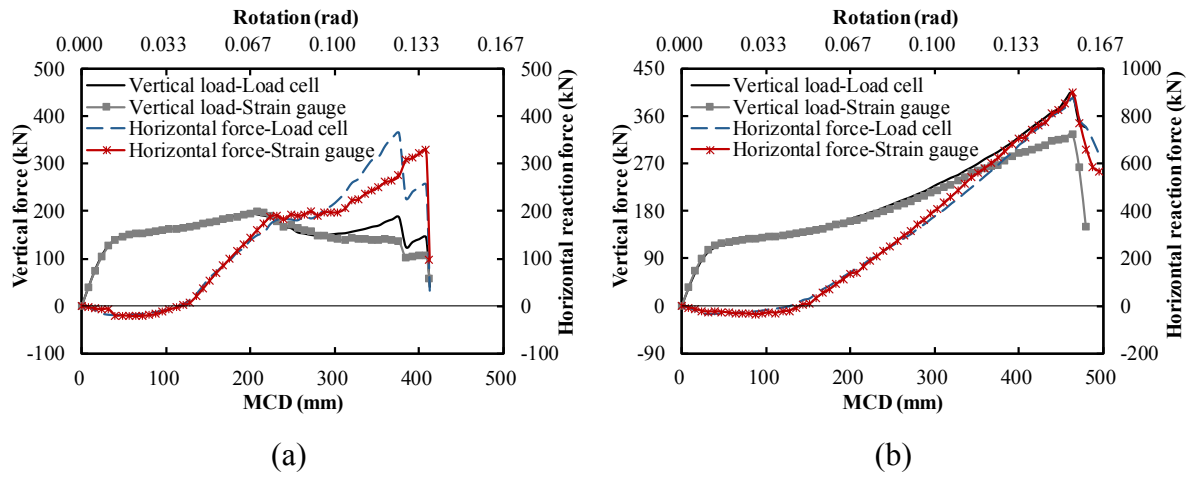
661
662
663 **Fig. 9** Overall deflection profile of the beams in the first story: (a) GBS; (b) RBS



667
668
669 **Fig. 10** Horizontal reaction force-middle column displacement curves: (a) GBS; (b) RBS

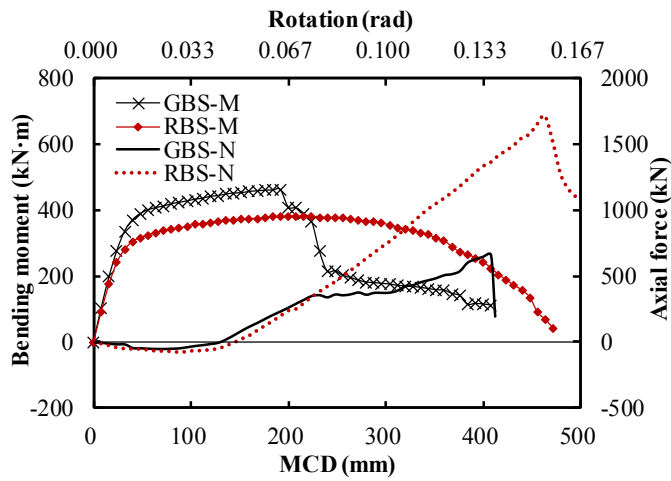


672
673 **Fig. 11** Internal forces at section B10 and B9



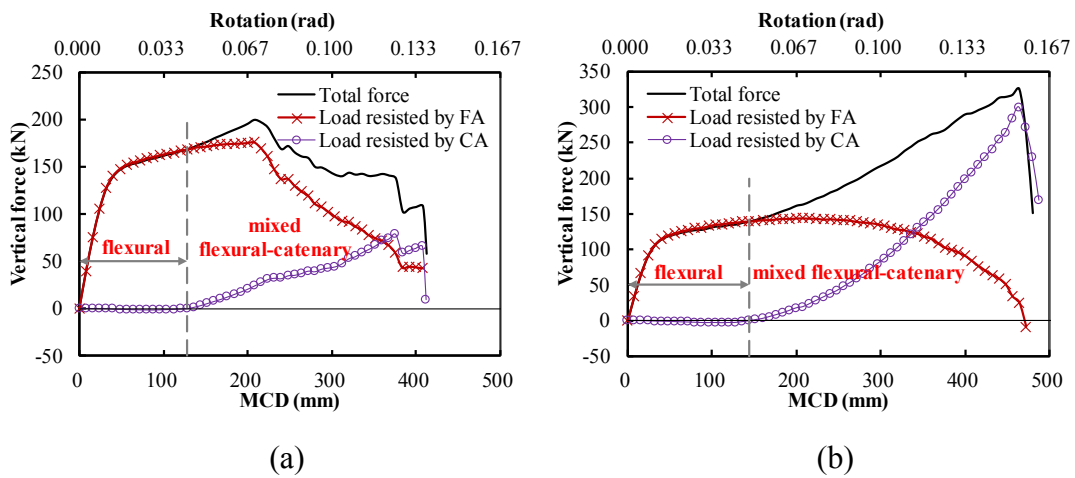
676
677
678
679
680
681

Fig. 12 Comparisons of vertical load resistance and horizontal reaction force from strain gauge and load cells: (a) GBS; (b) RBS



682
683
684
685

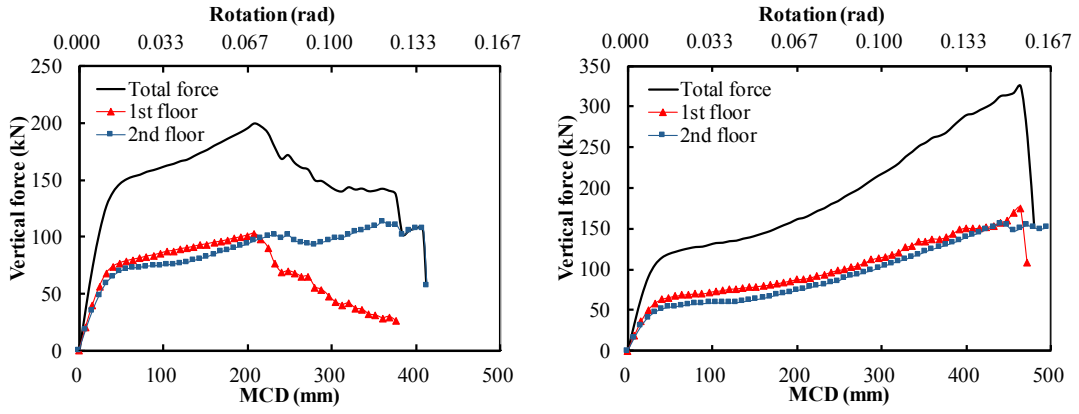
Fig. 13 Variation of total bending moment and axial force of GBS and RBS



686
687
688
689

Fig. 14 De-composition of the load resistance from different actions: (a) GBS (b) RBS
(Note: FA and CA represent flexural action and catenary action, respectively)

690



(a)

(b)

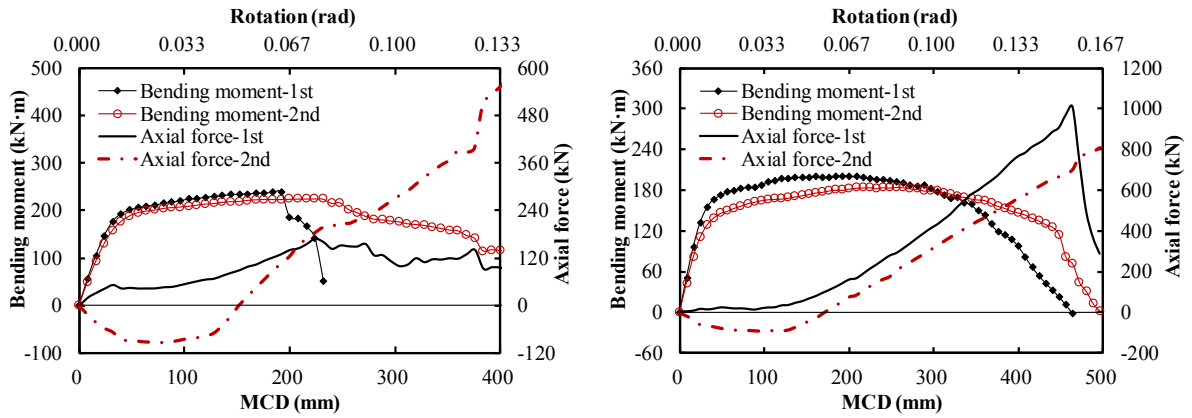
Fig. 15 De-composition of load resistance from 1st story and 2nd story: (a) GBS; (b) RBS

691

692

693

694



(a)

(b)

Fig. 16 Comparisons of the bending moment and axial force variation in 1st story and 2nd stories: (a)

GBS; (b) RBS

695

696

697

698

699

700

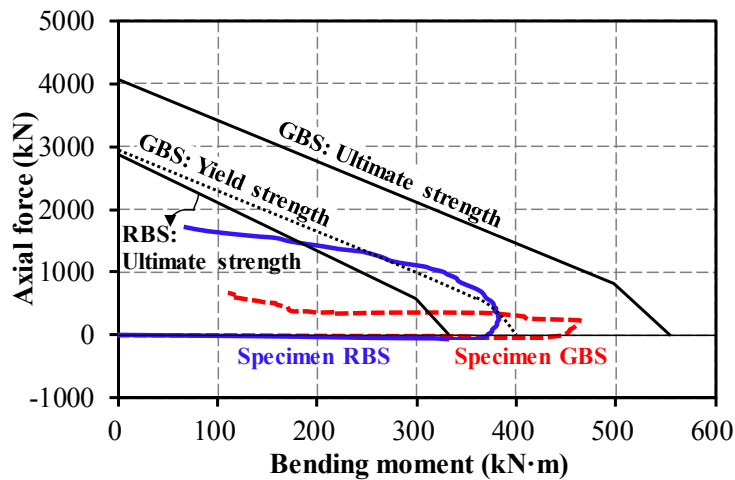


Fig. 17 Bending moment-axial force interaction diagram

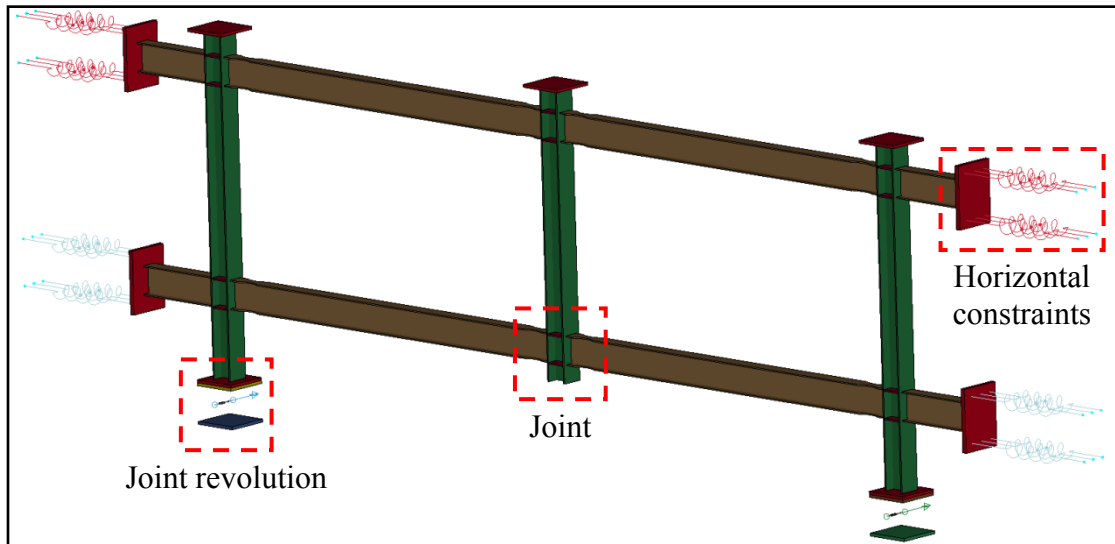
701

702

703

704

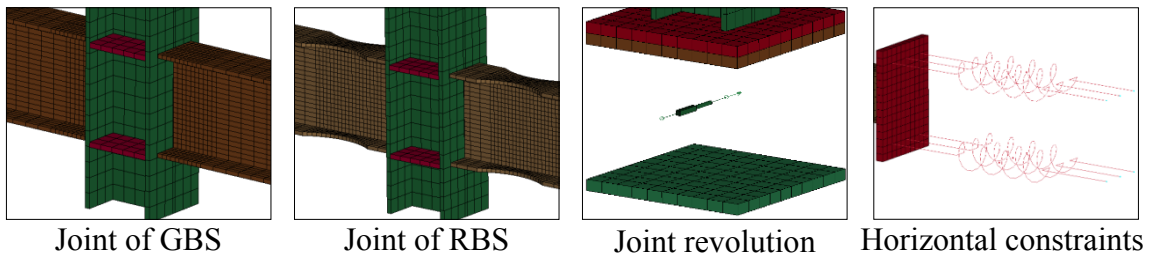
705



706

707

(a)



708

709

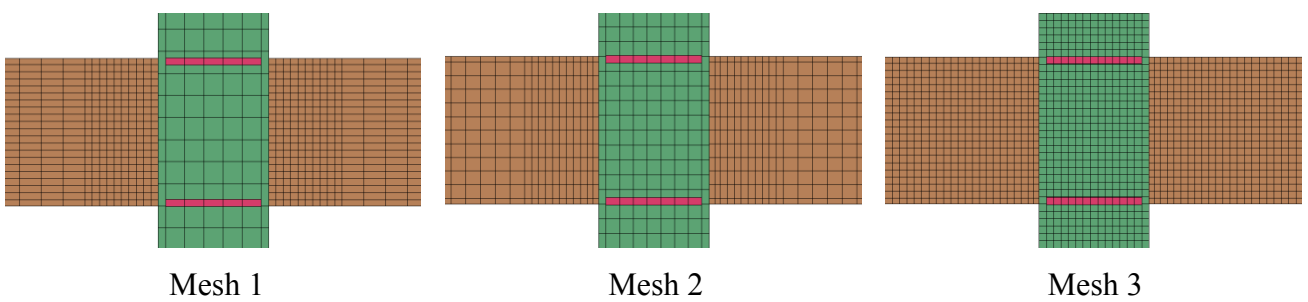
(b)

Fig. 18 Geometric model with boundary conditions: (a) overall view; (b) zone-in view

711

712

713



714

715

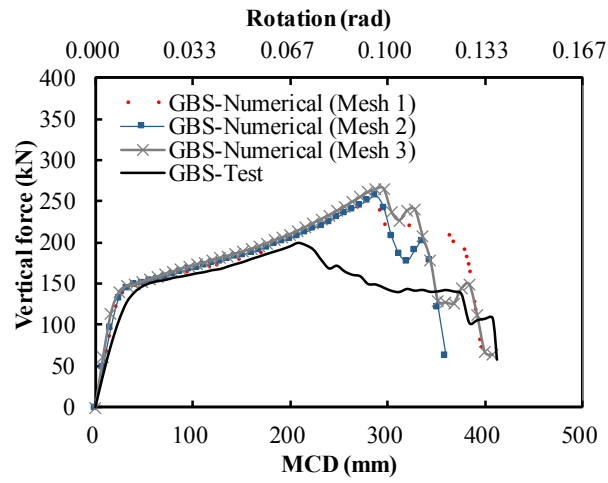
716

717

718

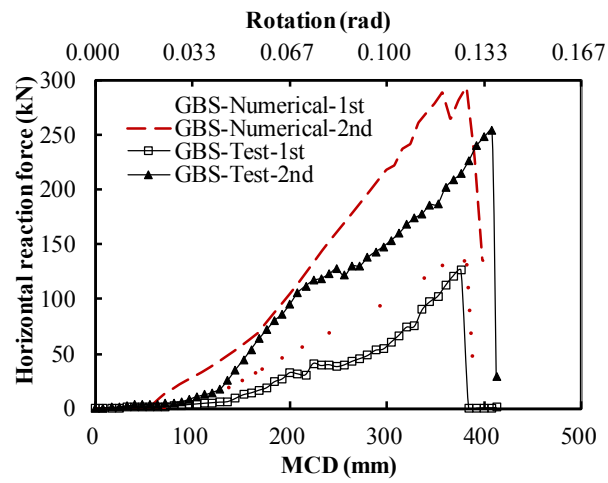
719

Fig. 19 Mesh configuration for different mesh strategy



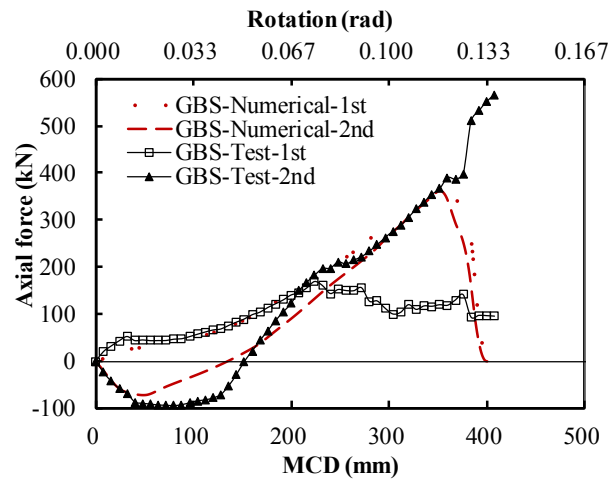
720
721

(a)



722
723

(b)

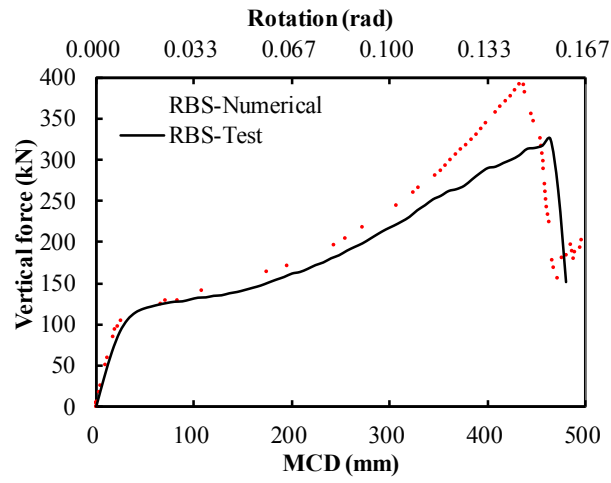


724
725

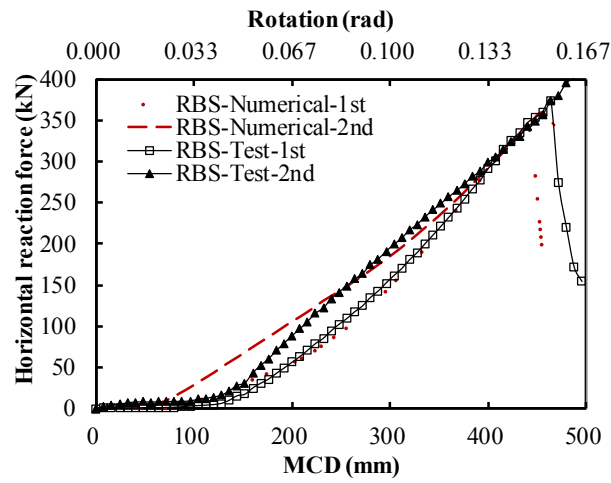
(c)

726 **Fig. 20** Comparison of experimental and numerical results of GBS: (a) vertical force; (b) horizontal
727 reaction force; (c) axial force in beams

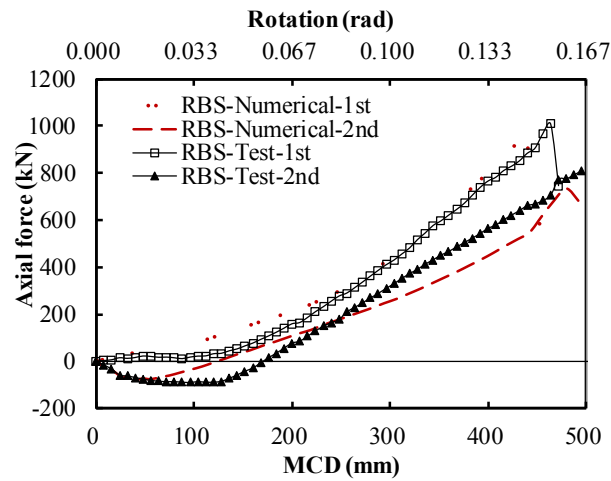
728
729
730



(a)

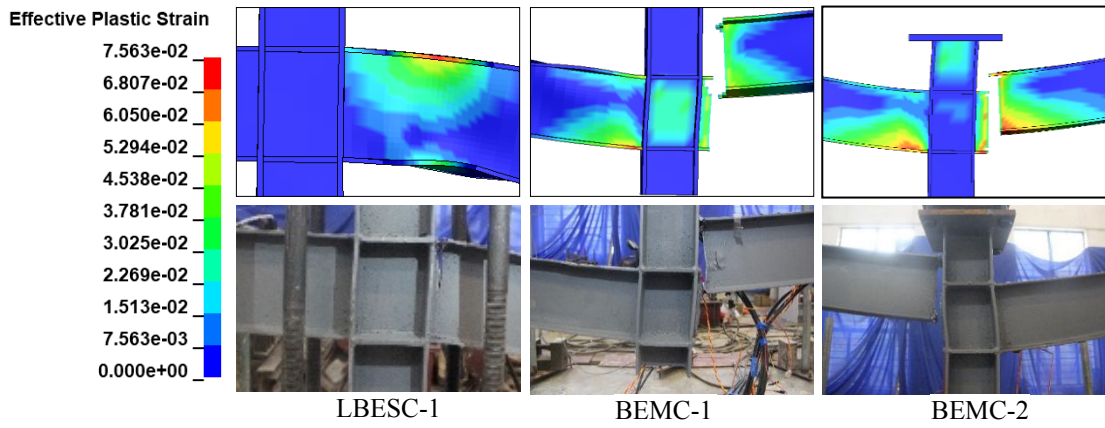


(b)



(c)

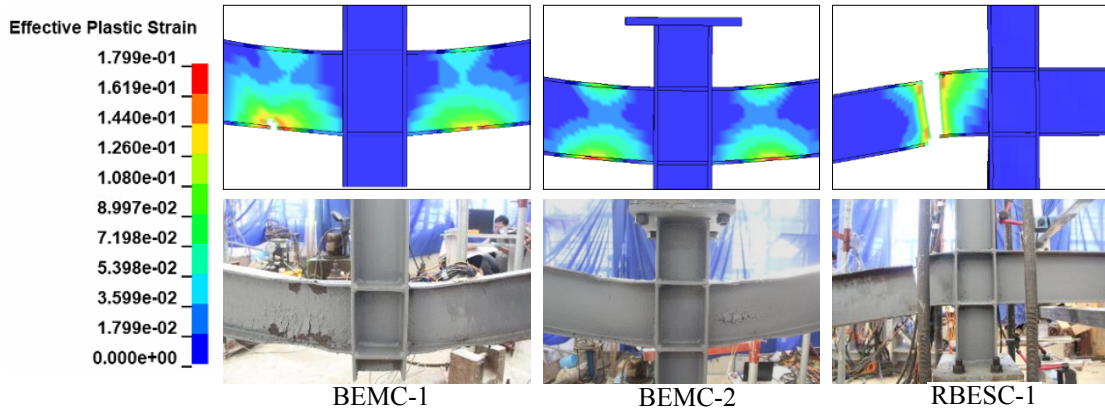
Fig. 21 Comparison of experimental and numerical results of RBS: (a) vertical force; (b) horizontal reaction force; (c) axial force in beams



742

743

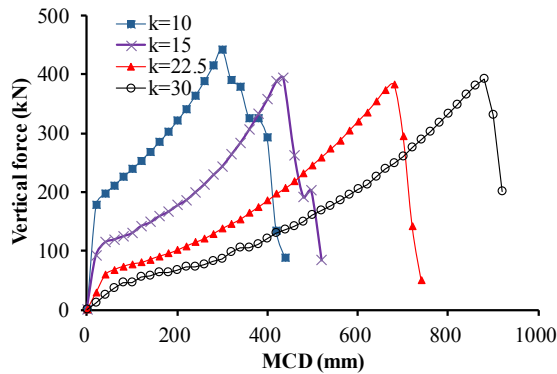
Fig. 22 Comparison of the failure mode of GBS from test and numerical model



744

745

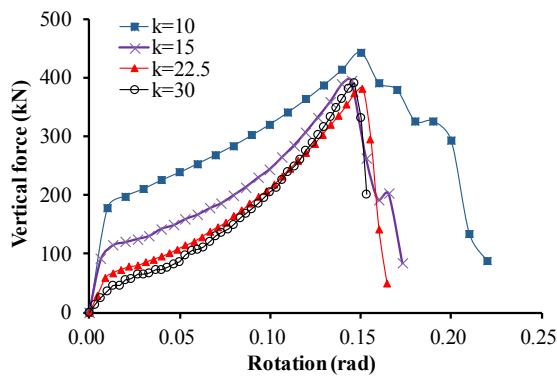
Fig. 23 Comparison of the failure mode of RBS from test and numerical model



746

747

(a)



748

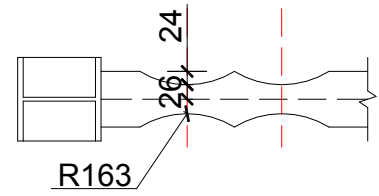
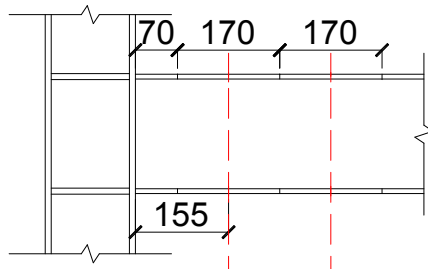
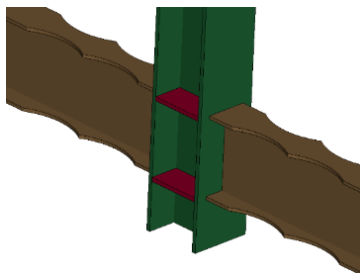
749

(b)

750

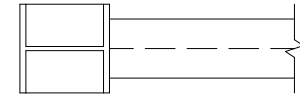
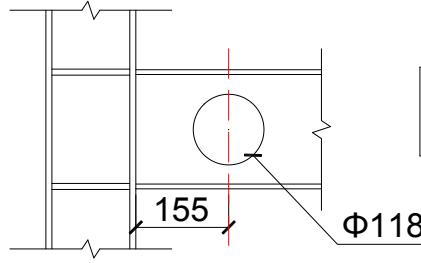
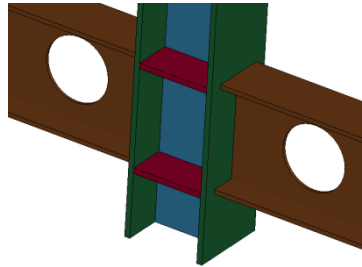
751

Fig. 24 Investigation on effects of span-depth ratio (k): (a) vertical force vs. MCD; (b) vertical force vs. Rotation



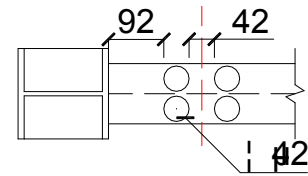
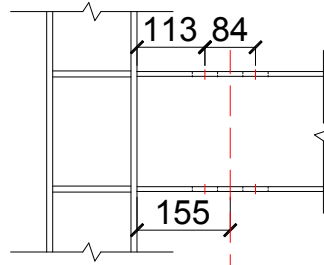
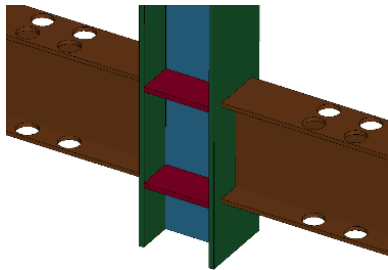
752
753

(a)



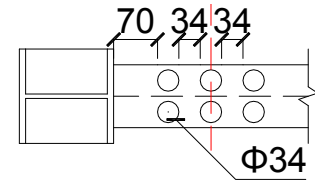
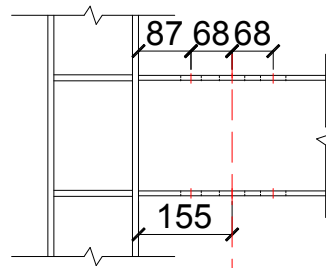
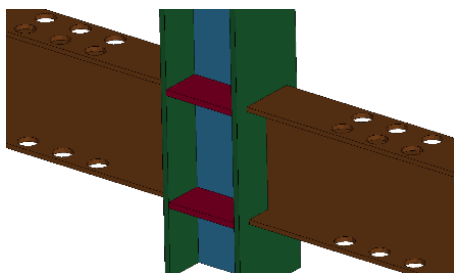
754
755

(b)



756
757

(c)

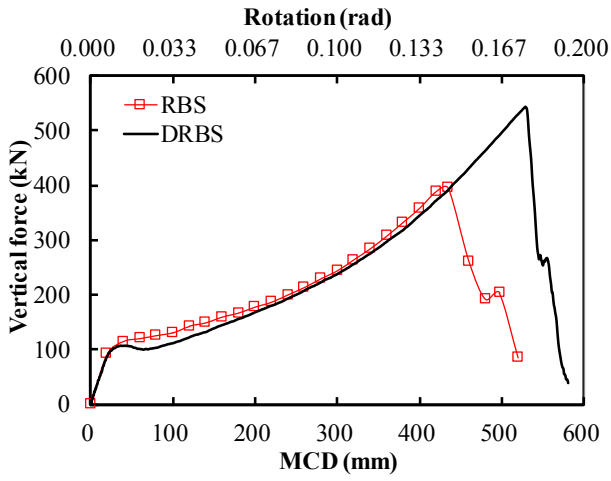


758
759

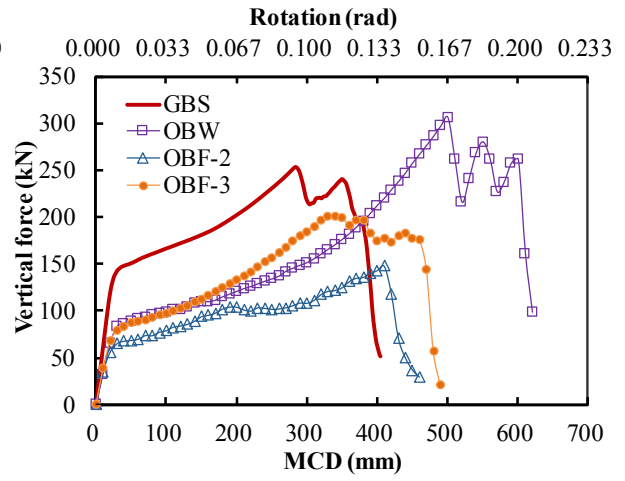
(d)

760 **Fig. 25** Details of different types of reduced beam section (unit in mm): (a) DRBS; (b) OBW; (c)
761 OBF-2; (d) OBF-3

762
763
764

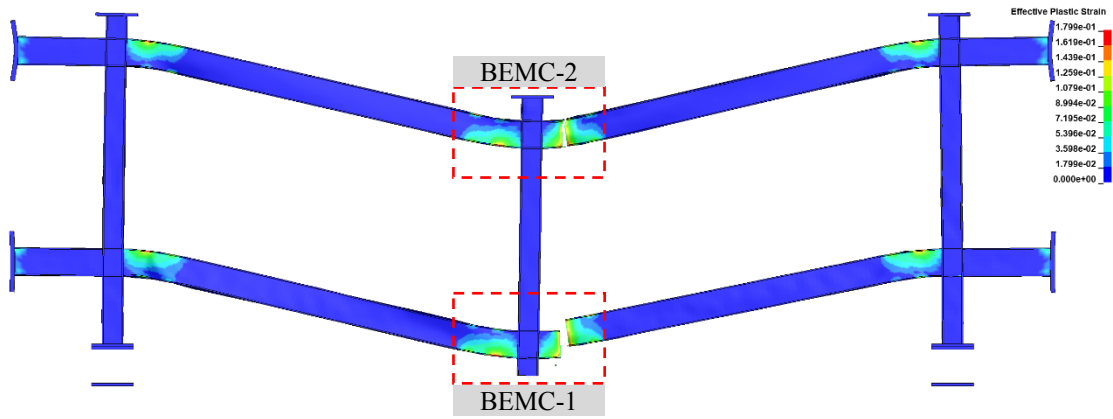


(a)

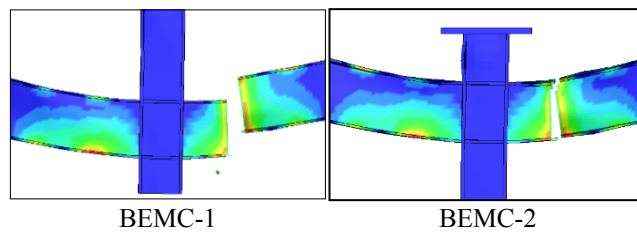


(b)

Fig. 26 Comparison of the load-displacement response: (a) RBS and DRBS; (b) GBS, OBW, OBF-2, and OBF-3

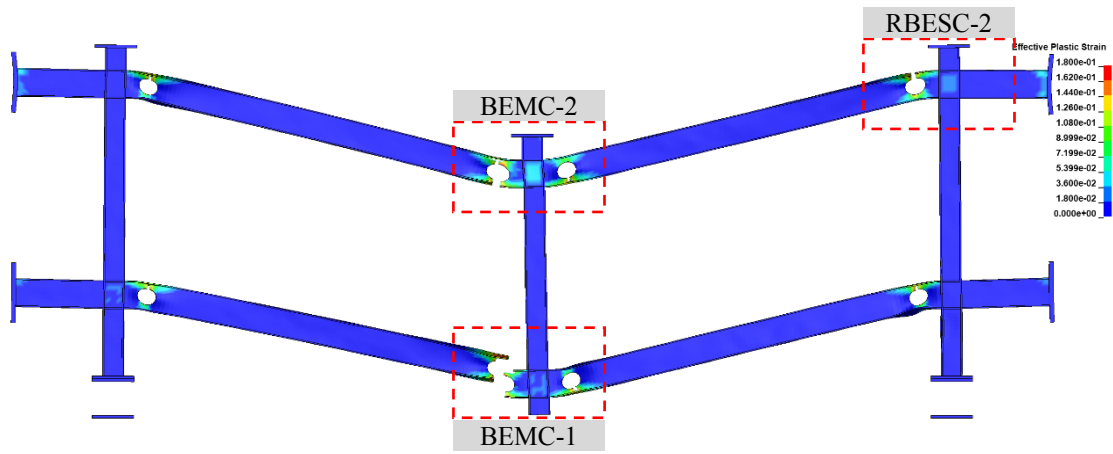


(a)

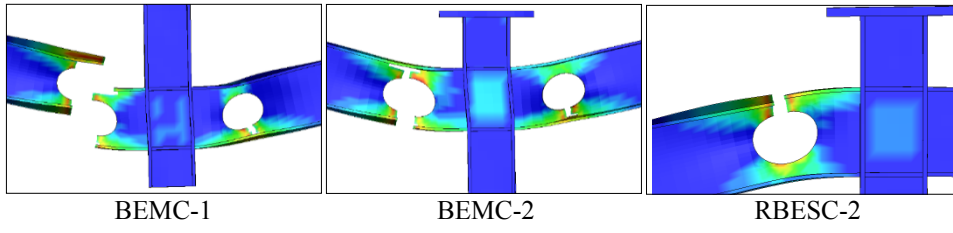


(b)

Fig. 27 Failure mode of DRBS: (a) overall view; (b) zone-in view

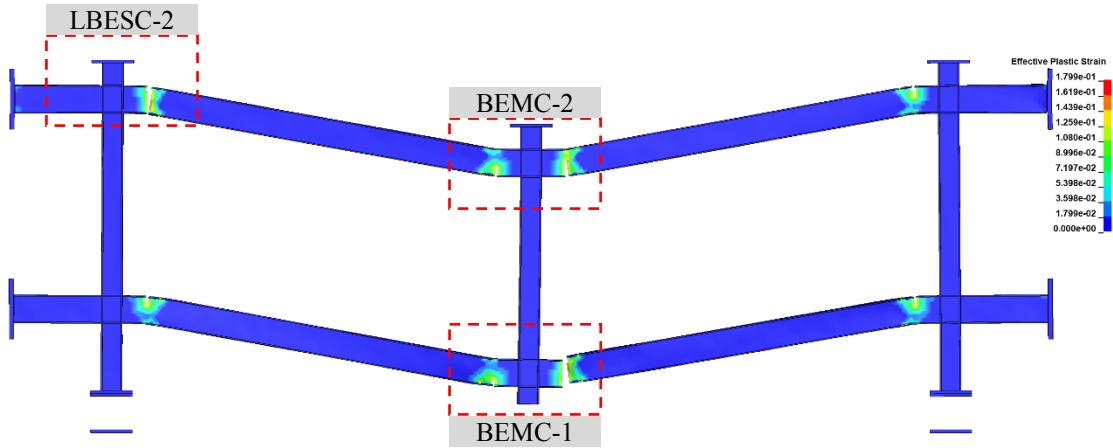


(a)

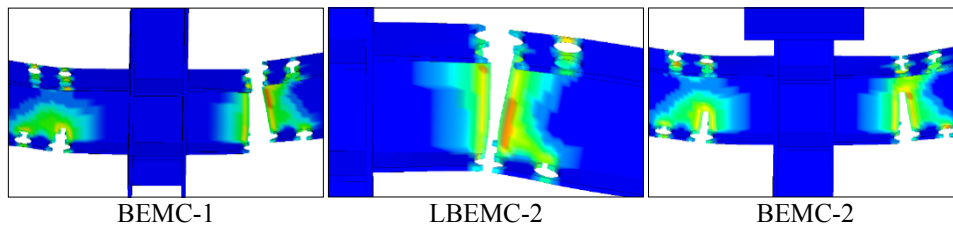


(b)

Fig. 28 Failure mode of OBW: (a) overall view; (b) zone-in view



(a)

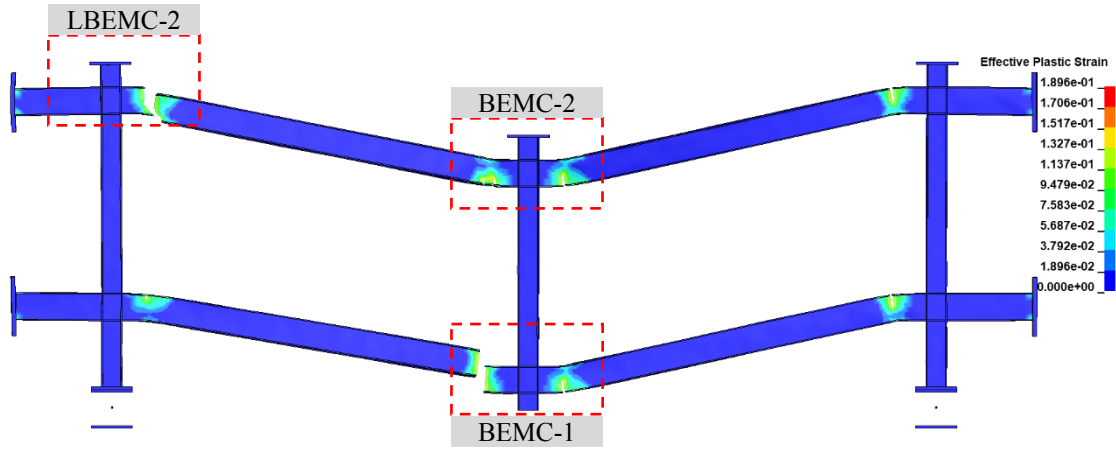


(b)

Fig. 29 Failure mode of OBF-2: (a) overall view; (b) zone-in view

793

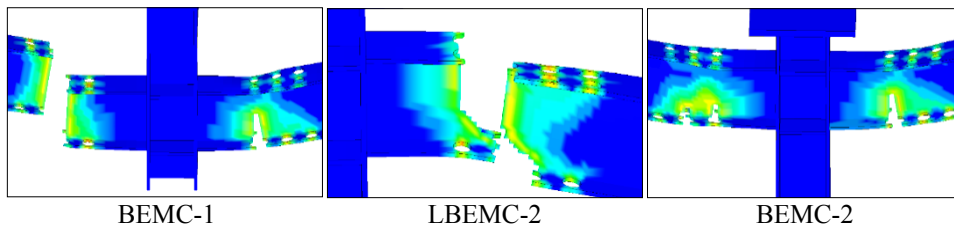
794



795

796

(a)



797

798

(b)

799

Fig. 30 Failure mode of OBF-3: (a) overall view; (b) zone-in view